SCIENCE CHINA
Chemistry

•REVIEWS•
SPECIAL ISSUE: In Honor of Professor Lixin Dai on the Occasion of His 100th Birthday

October 2023 Vol.66 No.10: 2754–2779
https://doi.org/10.1007/s11426-023-1725-8

Recent advances in metal-organic frameworks for oxygen evolution reaction electrocatalysts

Ming Liu[1†], Yin-Qiang Zhang[2†], Xuemin Wang[1], Feifan Lang[1], Na Li[2*] & Xian-He Bu[1,2*]

[1]*School of Materials Science and Engineering, Nankai University, Tianjin 300350, China;*
[2]*State Key Laboratory of Elemento-Organic Chemistry, College of Chemistry, Nankai University, Tianjin 300071, China*

Received June 23, 2023; accepted July 31, 2023; published online September 11, 2023

The anodic oxygen evolution reaction (OER) can be combined with various cathodic reactions to enable the electrochemical synthesis of diverse chemicals and fuels, particularly in water electrolysis for hydrogen production. It is however exhibiting a high overpotential due to the sluggish four-electron transfer process, which is considered the decisive reaction in energy conversion systems. In recent years, metal-organic frameworks (MOFs) have emerged as the ideal catalysts for accelerating OER. This is primarily because of their orderly porous architecture, structural tailorability, and compositional diversity. This review systematically summarizes the recent research progress in pristine MOF electrocatalysts for OER, which covers the construction strategies and electrocatalytic performance of more than eight types of MOFs. Additionally, the partial/complete structural reconstructions and their effects on MOF-based OER electrocatalysts are highlighted. In particular, the development process of "discovery, explanation, and utilization" for the structural reconstructions of MOF electrocatalysts is outlined. Furthermore, the catalytic mechanisms are elaborated in detail, aiming to provide insight into the rational design and performance optimization of MOF-based OER electrocatalysts. The challenges and future perspectives of MOF-based OER electrocatalysts for industrial applications are also discussed.

metal-organic frameworks, electrocatalysts, oxygen evolution reaction, structural reconstruction, active sites

Citation: Liu M, Zhang YQ, Wang X, Lang F, Li N, Bu XH. Recent advances in metal-organic frameworks for oxygen evolution reaction electrocatalysts. *Sci China Chem*, 2023, 66: 2754–2779, https://doi.org/10.1007/s11426-023-1725-8

1 Introduction

Developing efficient, low-cost, green, and sustainable energy systems is crucial for addressing the global energy crisis and related environmental issues [1–3]. Hydrogen energy, as a kind of secondary energy, has emerged as a potential driving force behind the global energy transition that possesses abundant sources, low-carbon emissions, high combustion calorific value (142 kJ/g), and wide applications [4–6]. Currently, traditional processes of hydrogen production, which rely on fossil fuels, have dominated the field due to their low cost. But their reliance on non-renewable resources and the resulting environmental pollution is incompatible with the concept of sustainable development [7]. In this context, electrocatalytic water splitting has become the key to the green and efficient production of hydrogen, offering significant advantages such as simple operation, high reaction efficiency, and pollution-free preparation process [8,9]. The water-splitting process involves two half-reactions, namely, the hydrogen evolution reaction (HER) at the cathode and the oxygen evolution reaction (OER) at the anode of the hydrolysis electrolyzer. Compared to the HER, the OER encounters challenges due to the multi-step proton-coupled electron transfer processes, resulting in slow kinetics and large overpotential, which hampers the overall efficiency of

†These authors contributed equally to this work.
*Corresponding authors (email: lina@nankai.edu.cn; buxh@nankai.edu.cn)

water splitting [10,11]. The existing noble metal-based catalysts like RuO_2 and IrO_2 feature high costs and poor stability, which limits the commercialization of hydrogen production through the water-splitting process [12,13]. Therefore, constructing new low-cost and high-efficiency OER electrocatalysts has become highly sought after.

Elucidating the catalytic mechanism of OER at the atomic/molecular levels as well as investigating the influence of various factors on the reaction kinetics is essential for the rational design of high-efficiency electrocatalysts [14]. Several crucial aspects should be considered. Firstly, the Sabatier principle emphasizes that the interaction between catalytic active centers and adsorbed intermediates in catalytic reactions plays a vital role in determining catalytic performance. This interaction hinges largely on the bonding and antibonding orbitals of the catalytic active centers and adsorbed intermediates. Thus, the electronic structure of the active centers in electrocatalysis is fundamental to achieving high OER activity. Secondly, fast and efficient charge transport is a cornerstone of excellent electrocatalytic activity. Thirdly, the presence of a suitable pore environment is another critical factor that affects catalyst performance. An ideal level of porosity in structure facilitates the adsorption/diffusion of reactive species, leading to improved utilization of active sites and accelerated mass transfer processes, thereby enhancing the catalytic activity. Fourthly, a well-defined structure helps in revealing the structural evolution process and structure-property relationships of active sites, which facilitates the rational construction of highly efficient OER electrocatalysts [15,16].

Metal-organic frameworks (MOFs) are ordered porous materials, assembled from metal nodes and organic ligands through coordination bonds, and have gained attention as promising candidates for electrochemical energy storage and conversion due to their modular design, molecular/atomic scale tunability, well-defined structure, large specific surface area, and variable pore environment [17–21]. However, such materials tend to feature high charge transfer energy barriers, resulting in poor electrical conductivity, thereby hindering their application in electrochemistry. To overcome this limitation, MOF materials are frequently used as template precursors to produce carbon-based composites for OER electrocatalysts [1,22,23]. Whilst some advances have been achieved using this approach, it still encounters certain limitations. For example, the carbonization process can easily destroy the pore structures of pristine MOFs, leading to the collapse of the ordered architecture. The aggregation of metal centers during calcination tends to yield multiphase catalysts, which greatly reduces the density of active sites over the product and hinders the establishment of structure-property relationships. Additionally, pyrolysis treatment often requires substantial energy consumption and generates gas pollution and organic ligand waste, thereby leading to a high industrial cost [24–26]. In contrast, an increasing number of pristine MOF materials have been developed as OER electrocatalysts. Versatile strategies have been proposed to enhance their OER activity, including the optimization of the metal-centered electronic structure *via* multimetal coordination, increse of the density of active centers through controlled crystallinity, improvement of MOF conductivity through the design of conjugated organic ligands, and achievement of functional synergy through multi-component composites. Sequentially, a series of MOF-based electrocatalysts with satisfactory performance have been achieved [27–29].

Although there are some recent reviews on the progress of MOF-based electrocatalysis, their attention focuses on MOF-derived carbon-based materials, two-dimensional MOFs, multimetallic MOFs, and composite MOFs, *etc.*, and the directions of the application are also focused on different electrocatalytic reactions [10,19–21]. There is a lack of reviews on pristine MOF electrocatalysts, especially OER electrocatalysts, while the systematic analysis of their catalytic mechanisms usually follows those of inorganic catalysts, and intrinsic catalytic mechanisms are often neglected. Particularly, the specificity of OER carried out in strongly alkaline oxidizing environments may cause the catalyst undergoing a certain degree of structural change, thereby leading to a more elusive catalytic mechanism. Therefore, it is urgent for a focused and comprehensive review regarding the structural properties, compositional modulation, morphological design, electrocatalytic performance, and catalytic mechanism of MOF OER electrocatalysts. Especially importantly, a systematic elucidation of the catalytic mechanism is imminent to provide strong guidance for the design and construction of MOF OER electrocatalysts.

Herein, we focus on the most recent advances in pristine MOF electrocatalysts for OER with emphasis on new construction strategies and OER performance, especially understanding their structure-property relationship. Firstly, the design and construction of MOF electrocatalysts, including the design of metal centers, ligand modification, morphology modulation, crystallinity regulation, functional composites, and array assembly of conducting substrates, are summarized in detail, and especially, the performance of representative MOF-based OER electrocatalysts in the last 2–3 years are analyzed. Most importantly, the partial/complete structural reconstruction processes of MOF-based OER electrocatalysts are carefully outlined, whilst delving into the catalytic mechanisms to clarify some existing ambiguities in the field. Lastly, the main challenges associated with designing and preparing MOF-based OER electrocatalysts are also discussed (Scheme 1). This progress report aims to open up new avenues for the structural design, electrocatalytic mechanisms, and practical applications of MOF OER electrocatalysts.

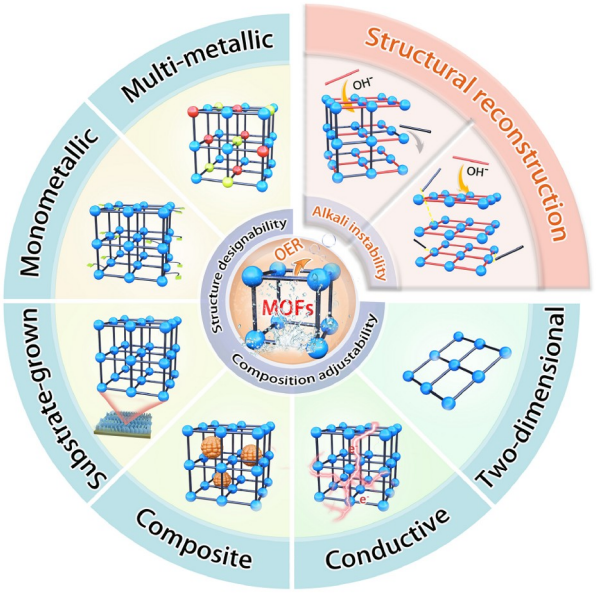

Scheme 1 Illustration of designing advanced MOF electrocatalysts for OER (color online).

2 Oxygen evolution

2.1 Reaction mechanism

The OER undergoes four-electron transfer steps with multiple oxygen-containing reactive intermediates. The theoretical Gibbs free energy change (ΔG) of each step is 1.23 eV. However, in the actual OER reaction process, the Gibbs free energy of each step may change owing to the uncontrollable factors of intermediates generated in each step (*i.e.*, $\Delta G >$ 1.23 eV or $\Delta G <$ 1.23 eV) [30]. Therefore, among the four electron steps, the step with the largest ΔG is considered the rate-determining step in OER. This indicates that the highest energy barrier is required to be overcome to drive the catalytic reaction. The difference between the Gibbs free energy of the rate-determining step and the theoretical step determines the overpotential of the entire OER reaction. In the past decade, researchers have developed various descriptors based on theoretical calculations, such as d-band center, p-band center, and e_g electron orbital filling, for predicting the OER performance [31–33]. Taking e_g as an example, Shao-Horn *et al*. [31] constructed a volcano diagram of the B-site metal, e_g electron filling, and reactivity from a large number of ABO_3 perovskite oxides and indicated that the adsorption is optimal. The best performance can be obtained when the e_g electron filling was 1. The e_g electron filling was less than 1, and the adsorption of oxygen intermediates became stronger, which was unfavorable for the desorption of reactants; as e_g electron filling was greater than 1, the adsorption of oxygen intermediates became weaker. However, e_g electron filling also has some limitations. For example, e_g electron filling cannot be used to elucidate $LaMnO_3$, $LaCoO_3$, and $LaNiO_3$ catalysts with the same e_g orbital occupancy but different OER activities. This was mainly limited by the fact that the e_g orbital filling theory based on an ionic model failed to reflect the covalency of the metal-oxygen bond [34]. Therefore, a single descriptor is insufficient but in combination with multiple descriptors can accurately predict catalytic activities. As a guide, the oriented optimization of the catalysts in terms of d-band center, e_g electron filling, and coordinatively unsaturated metal cations through various strategies, including structural modulation, component compounding, and ion doping, is expected to deliver high OER electrocatalytic activities.

In addition, several parameters, including overpotential, Tafel slope, turnover frequency, electrochemically active area, mass activity, stability, and faraday efficiency, have been used to evaluate the electrocatalytic performance of OER. Overpotential refers to the difference between the externally applied potential and the theoretical potential, and the overpotential with a current density of 10 mA cm^{-2} is usually chosen as an evaluation indicator; Tafel slope indicates the kinetic properties of the catalyst; turnover frequency indicates the intrinsic catalytic activity of the catalyst; electrochemically active area can only indicates the area of the active area with the potential of catalytic activity, not the area where the catalytic reaction actually occurs; mass activity refers to the current density normalized to the loading of the target catalyst at a specific overpotential; stability is employed to evaluate the cycling durability of the catalyst; faraday efficiency is performed to analyze the efficiency of energy conversion in the catalytic process.

Currently, the two widely recognized reaction mechanisms are the conventional adsorbate evolution mechanism (AEM) and the lattice oxygen-mediated mechanism (LOM), respectively (Figure 1) [35,36]. In AEM, the single metal center works as the active site, and the reaction involves three oxygen-containing intermediates, namely, O^*, OH^*, and OOH^*, which are formed from adsorbed water molecules or hydroxyl radicals. The study showed that some correlations existed between the Gibbs free energy of different intermediates. The difference between Gibbs free energy of OH^* and OOH^* was an approximate constant of around 3.2 eV, and this linear correlation property corresponded to the similar M–O bond adsorption conformation of M-OH^* and M-OOH^* [33]. Nørskov *et al*. [30] revealed a volcanic relationship between the theoretical overpotential of oxide catalysts and the difference between ΔG_O^* and ΔG_{OH}^*. Hence, $\left(\Delta G_O^* - \Delta G_{OH}^*\right)$ can be considered a generic descriptor for the OER activity. However, this thermodynamic constraint makes it possible to optimize the adsorption of intermediates only to a small extent, with a theoretical minimum overpotential of only 370 mV, which can hardly be further enhanced.

For LOM, the oxygen atoms as the active site in the cat-

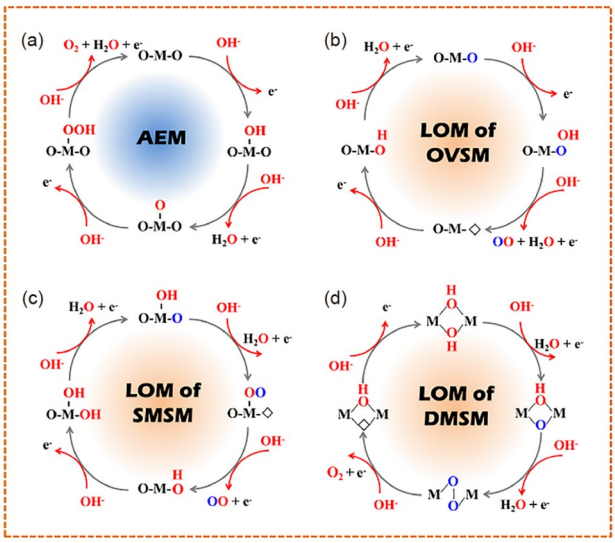

Figure 1 Schematic diagram of (a) AEM mechanism and LOM of (b) OVSM, (c) SMSM, and (d) DMSM mechanism for OER (color online).

alyst lattice participate in the OER and form oxygen vacancies during the reaction process [11,37]. First, OH^- was adsorbed on the surface of the catalyst, and a deprotonation reaction occurred, forming two adjacent O intermediates. Subsequently, these two adjacent intermediates directly reacted and coupled to form O–O intermediates, giving rise to O_2 (Figure 1b). Unlike AEM, LOM involves the migration, and coupling of lattice oxygen, as well as the generation of oxygen vacancies. Moreover, oxygen as the active site can break the linear limitation of AEM, avoiding the generation of high-energy barriers *OOH, further achieving enhanced performance. The rate of oxygen production in the presence of LOM is closely correlated to the electronic structure of the catalysts and depends on the covalent bond strength of metal-oxygen species. In addition, the d-band center theory is amenable to establishing a dependency between the electronic structure of d orbitals of transition metal elements and the adsorption strength of OER intermediates, thus serving to predict the theoretical activity of catalysts [38]. However, the fatal drawback of LOM occurring during the reaction is its structural instability, which is caused by the involvement of lattice oxygen in OER. Therefore, the balance of the high structural stability and low activity of AEMas well as the low structural stability and high activity of LOM has become the focus of this field.

Further, LOM has also developed into an oxygen-vacancy-site mechanism (OVSM), single-metal-site mechanism (SMSM), and dual-metal-site mechanism (DMSM) depending on the different active sites (Figure 1c, d) [39]. Other mechanisms, including coupled oxygen evolution mechanism and oxide path mechanism, have also been developed and used to design efficient OER electrocatalysts [40,41].

2.2 MOFs as OER electrocatalysts

Electrocatalysts stand at the heart and are the key to achieving efficient electrocatalytic reactions. Although a large variety of transition metal compounds have been explored as OER electrocatalysts, their industrial application is still limited by the catalyst activity and stability. Therefore, it is urgent to develop efficient OER electrocatalysts. MOFs are a family of porous crystalline materials with flexible chemical and structural adjustability. Owing to their long-range order, synthetic diversity, innate porosity, and host-guest chemistry, MOFs are desirable platforms for constructing advanced OER electrocatalysts [42–44]. The modular nature of MOFs endows them with high synthetic tunability, providing precise compositional and structural control. The dominant natures of pristine MOFs for the OER process, including porosity, stability, conductivity, and morphology, can be tuned using synthetic designs. The nature of the long-range order of MOFs provides abundant redox-active metal centers and functionalized organic ligands, which facilitates electron transfer during OER, thereby significantly enhancing the utilization of atoms and intrinsic activity of the material. The crystalline nature of MOFs facilitates the identification of active centers and the elucidation of structure-property relationships. The innate porosity of MOFs is also highly vital for guest introduction and electron/ion transfer. This allows for the encapsulation of active species to improve the OER activity and provide significant interfacial contact with the electrolyte solution to facilitate mass transport. Both electron and mass transport are essential for the OER process and directly affect the overpotential and efficiency of OER catalysts. Furthermore, the excellent stability of the MOFs further promotes cycling capabilities. Notably, most MOFs feature inherently low conductivity owing to the blockage of their active centers by the surrounding organic ligands and poor electron interactions between the organic ligands and the metal centers, which limits their electrocatalytic OER performance. The direct use of pristine MOFs as electrocatalysts for OER remains in the infancy stage. Recently, significant research efforts are aimed at tailoring the properties of MOFs to improve the conductivity and OER activity of pristine MOFs, while numerous MOF OER catalysts with different properties have been developed, facilitating the targeted construction of high-performance OER electrocatalysts (Figure 2) [45–53].

3 Design concepts of pristine MOFs

MOFs have been widely studied and explored as efficient OER electrocatalysts. In the past decades, several rational design concepts have been proposed to construct MOFs for

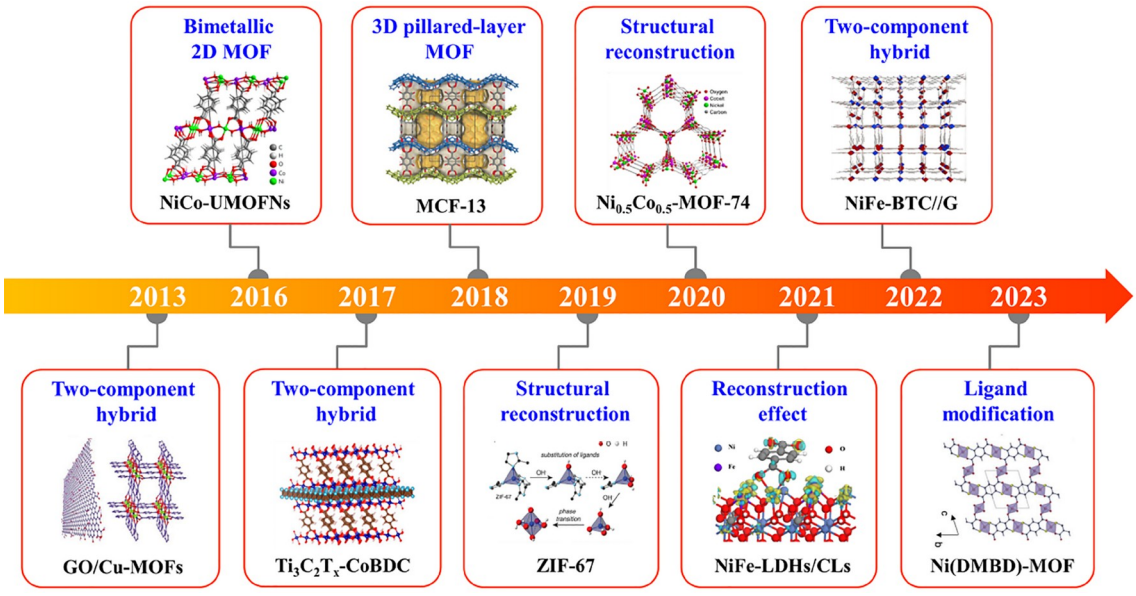

Figure 2 Timeline shows representative research progress of pristine MOF materials as OER catalysts. Reprinted with permission from Ref. [45], Copyright©2013 John Wiley & Sons, Inc.; Ref. [46], Copyright©2016 Springer Nature; Ref. [47], Copyright©2017 American Chemical Society; Ref. [48], Copyright©2018 John Wiley & Sons, Inc; Ref. [49], Copyright©2019 American Chemical Society; Ref. [50], Copyright©2020 Springer Nature; Ref. [51], Copyright©2021 John Wiley & Sons, Inc; Ref. [52], Copyright©2022 Springer Nature; Ref. [53], Copyright©2023 John Wiley & Sons, Inc. (color online).

improving OER catalytic performance. In this chapter, we introduced design concepts to improve the OER catalytic performance of different types of MOFs. Furthermore, some representative performances of MOF OER electrocatalysts in the last 2–3 years are listed at the end of this section (Table 1).

3.1 Monometallic MOFs

For MOFs based on only single metal, the metal site is typically a transition metal with 3d unoccupied orbitals, which can accommodate foreign electrons and reduce the binding energy of oxygen-containing intermediates such as O^* and OOH^* [81]. Single metal sites as active centers can often be modified using ligands and structural designs to improve their OER electrocatalytic performance [82–85]. For example, the coordination of different organic ligands can induce the optimization of the electronic structure of the metal active centers, while the post-treatment can also change the coordination configuration of the metal active centers and optimize the binding energy of the oxygen-containing reaction intermediates for enhancing the electrocatalytic activity.

The coordination environment of the metal active centers often determines the electrocatalytic activity. Li *et al*. [86] prepared a Co-based MOF, $[Co_2(\mu\text{-}Cl)_2(bbta)]$ (MAF-X27-Cl, H_2bbta = 1*H*,5*H*-benzo-(1,2-d:4,5-d′)bistriazole) with high stability as the OER candidate material. Then the isostructural MAF-X27-OH was obtained by complete substitution of Cl^- on MAF-X27-Cl by OH^- *via* linear sweep voltammetry (LSV) activation treatment. Under neutral conditions, MAF-X27-OH exhibited superior OER activity and a larger electrochemical surface area than MAF-X27-Cl. Isotope tracking experiments suggested that the μ-OH^- ligand participated in the OER process, thereby reducing the reaction energy barrier. In 2022, Hou *et al*. [57] constructed a CoBDC FcCA (H_2BDC = terephthalic acid) catalyst comprised of two kinds of different metal sites and ferrocene carboxylic acid (FcCA). This catalyst featured an ultrathin nanosheet structure and displayed excellent OER performance with a low overpotential of 280 mV at 10 mA cm^{-2}. It was shown that the introduction of FcCA induced the formation of two types of Co sites (Figure 3a). One active site was directly coordinated to FcCA and the other was an unsaturated site, the former achieved enhanced OH^* adsorption energy of the metal sites, while the latter reduced the spin state of the Co sites and the formation energy of the key reaction intermediate OOH^*, thus improving the catalytic activity. Rational modification of organic ligands can change the coordination environments of metal centers to optimize the electronic structure, thus achieving significant improvement in electrocatalytic performance (Figure 3b, c). Zhu *et al*. [53] developed a versatile system of Ni-MOF electrocatalysts by utilizing a thiol-functionalized 2,6-dimercaptanbenzene-1,4-dicarboxylate (DMBD) linker, in which Ni–S was integrated into the coordination chains to functionalize the MOF scaffolds (Figure 3d, e). Theoretical calculations and experimental results showed that Ni(DMBD)-MOF displayed metallic electronic band structure due to the Ni–S coordination, which enhanced the conductivity compared with non-thiol (*e.g.*, 1,4-benzenedicarboxylic acid) analogs

Table 1 Summary of different types of MOF electrocatalysts used in OER in recent years

Catalyst	Overpotential (mV@mA cm^{-2})	Tafel slope (mV dec^{-1})	Binder	Electrolyte (KOH)	Substrate	Metal centers	Modification strategy	Stability
Co-BTC-IMI [54]	360@10	88	Nafion	0.1 M	RDE [b]	Co	Coordination environment	12,000 s@5 mA cm^{-2}
MOF3_A [55]	425@10	99	Nafion	0.5 M	GCE [c]	Co	Coordination environment	N/A
$[Co_7(t\text{-}ca)_{14}(H_2O)_2]$ [56]	361@10	28	Nafion	0.1 M	GCE	Co	Structural modulation	10,000 s@10 mA cm^{-2}
CoBDC FcCA [57]	280@10	53	N/A [a]	1.0 M	N/A	Co	Coordination environment	40,000 s@1.6 V *vs.* RHE
Rbf-Ni-MOF [58]	220@10	52	Nafion	1.0 M	GCE	Ni	Coordination environment	24 h@10 mA cm^{-2}
NiFc-MOF/NF [59]	195@10	44.1	None	1.0 M	NF [d]	Ni	Coordination environment	40 h@10 mA cm^{-2}
CSMCRI-19 [60]	350@10	35.4	Nafion	1.0 M	CC [e]	Ni	Coordination environment	N/A
NiFe(dobpdc) [61]	207@10	40	None	1.0 M	NF	Ni, Fe	Topography regulation	30 h@10 mA cm^{-2}
$Co_{0.9}Ce_{0.1}$-BTC [62]	308@10	107	Nafion	1.0 M	GCE	Co, Ce	Multimetallic synergy	25 h@10 mA cm^{-2}
CoCu-MOF NBs [63]	271@10	63.5	None	1.0 M	NF	Co, Cu	Multimetallic synergy	100 h@N/A
Fe-Co-Ni MOF [64]	254@10	51.3	N/A	1.0 M	RDE	Fe, Co, Ni	Multimetallic synergy	48 h@100 mA cm^{-2}
Fe_2V-MOF [65]	314@10	58	None	1.0 M	NF	Fe, V	Multimetallic synergy	12 h@10 mA cm^{-2}
Fe-CoNi MOFs [66]	230@10	53.7	None	1.0 M	NF	Fe, Co, Ni	Multimetallic synergy	100 h@10 mA cm^{-2}
NiFe-btz films [67]	239@10	44.3	None	1.0 M	NF	Fe, Ni	Multimetallic synergy	12 h@~9 mA cm^{-2}
ZIF-62-(Co)-Fe-CC [28]	335@10	N/A	None	0.1 M	CC	Fe, Co	Multimetallic synergy	200 h@10 mA cm^{-2}
NiFe-MOF [68]	240@10	73.44	Nafion	1.0 M	GCE	Fe, Ni	Topography regulation	16 h@10 mA cm^{-2}
Fe-doped-(NiMOFs)/FeOOH [69]	210@15	50	None	1.0 M	NF	Fe, Ni	Multicomponent synergy	120 h@10 mA cm^{-2}
NiFe-MOF//G [52]	106@10	55	None	1.0 M	Graphite foil	Fe, Ni	Conductivity optimization	150 h@10 mA cm^{-2}
$BaTiO_3$@MOF-Fe/Co [70]	247@10	38.4	Nafion	1.0 M	GCE	Fe, Co	Multicomponent synergy	10 h@247 mV
CeO_2@NiFe-MOFs [71]	248@20	46	N/A	1.0 M	GCE	Ce, Fe, Co	Multicomponent synergy	40 h@20 mA cm^{-2}
MTV-MOFs [72]	286@10	45.3	Nafion	1.0 M	Carbon paper	Fe, Ni	Coordination environment	16,000 s@10 mA cm^{-2}
Ni(DMBD)-MOF/NF [53]	295@10	32	None	1.0 M	NF	Ni	Coordination environment	100 h@100 mA cm^{-2}
NiYCe-MOF/NF [73]	245@10	65	None	1.0 M	NF	Ni, Y, Ce	Multimetallic synergy	100 h@200 mA cm^{-2}
$V_{0.09}Ni_{0.91}$MOF/NF [74]	235@10	30.3	None	1.0 M	NF	V, Ni	Multimetallic synergy	80 h@400 mA cm^{-2}
Ni-BDC/Fe [75]	279@100	52.1	None	1.0 M	IF [f]	Ni, Fe	Multimetallic synergy	100 h@400 mA cm^{-2}
Fe-B/Fe-MOF/IF [76]	210@10	38	None	1.0 M	IF	Fe	Multicomponent synergy	100 h@500 mA cm^{-2}
FeNi-MOF [77]	239@50	52.4	None	1.0 M	NF	Fe, Ni	Multimetallic synergy	200 h@500 mA cm^{-2}
MFN-MOFs/NF [78]	235@50	55.4	None	1.0 M	NF	Fe, Ni	Multimetallic synergy	100 h@500 mA cm^{-2}
Fe_{MOFs}-SO_3 [79]	218@10	36.2	N/A	1.0 M	NF	Fe	Coordination environment	100 h@1,000 mA cm^{-2}
FCN-MOF/NF [80]	196@10	29.5	None	1.0 M	NF	Fe, Co, Ni	Multimetallic synergy	50 h@1,000 mA cm^{-2}

a) N/A means not available; b) RDE means rotating disk electrode; c) GCE means glassy carbon electrode; d) NF means Ni foam; e) CC means carbon cloth; f) IF means Fe foam.

(BDC)-MOF. This optimized structure facilitated the generation of O^* intermediates, leading to satisfactory electrocatalytic activity for the OER (Figure 3f–h).

As a classical MOF material, zeolitic imidazolate framework-67 (ZIF-67) was widely applied due to its facile synthesis and structural stability. However, the OER performance of this material is undesirable because the complete coordination of Co ions in ZIF-67 leads to the scarcity of active sites. In order to activate the Co ions and convert them into catalytic active sites, Wang *et al.* [87] constructed metal centers with coordination unsaturation in ZIF-67 (CUMSs-ZIF-67) by plasma etching and removing integrant organic ligands. The CUMSs-ZIF-67 exhibited significantly enhanced OER activity compared with the pristine ZIF-67 in near-neutral (0.5 M KBi) and basic (1.0 M KOH) electrolytes. Density functional theory (DFT) calculations confirmed that the high activity caused by unsaturated metal sites was attributed to the strong interaction of the highly

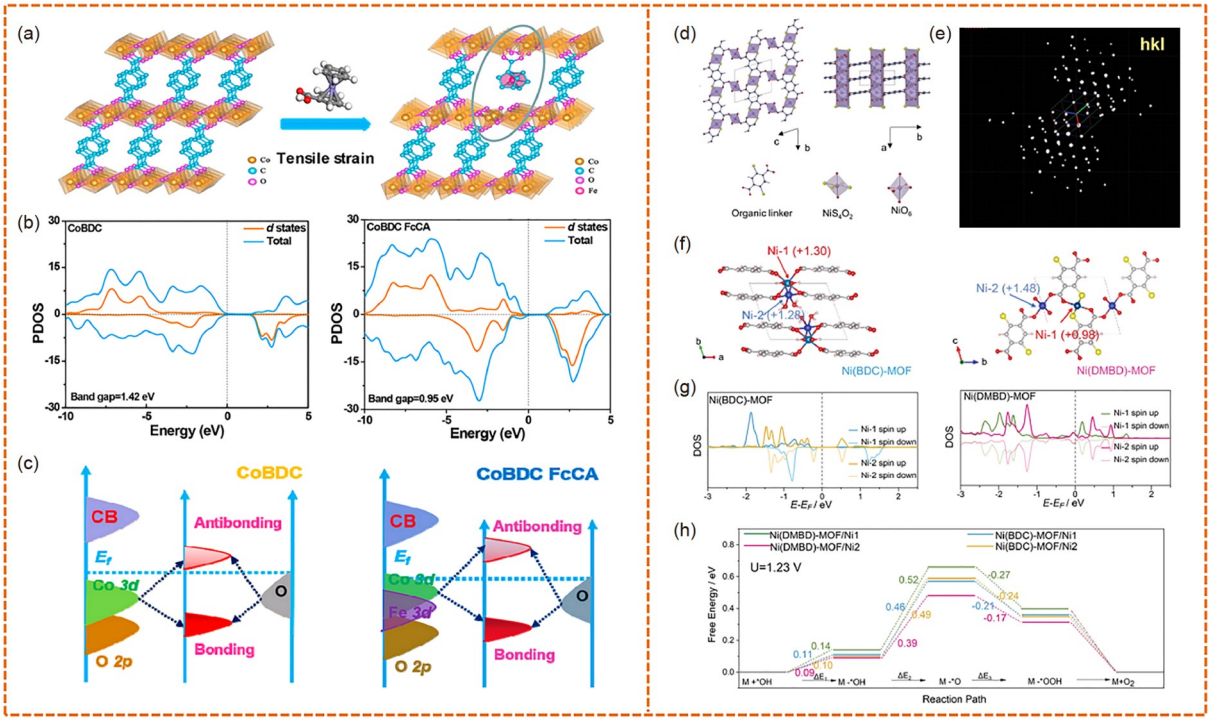

Figure 3 (a) Structural schematic diagrams and (b) calculated partial density of states (PDOS) of CoBDC and CoBDC FcCA models. (c) The schematic diagram of the bond formation between the Co and O of CoBDC and CoBDC-FcCA models. Reproduced with permission from Ref. [57], Copyright©2022 American Chemical Society. (d) Structural schematic diagrams, (e) 3D reciprocal lattices of Ni(DMBD)-MOF. (f) The Ni sites in Ni(BDC)-MOF and Ni(DMBD)-MOF. (g) DOS of Ni in Ni(BDC)-MOF and Ni(DMBD)-MOF calculated by DFT. (h) The calculated free energy diagrams of the OER process on Ni(BDC)-MOF and Ni(DMBD)-MOF. Reproduced with permission from Ref. [53], Copyright©2023 John Wiley & Sons, Inc. (color online).

positively charged metal component with oxygen, which optimized the adsorption of oxygen-containing intermediates and activated the OER active centers.

3.2 Multi-metallic MOFs

Compared with monometallic MOF materials, multi-metallic MOFs have attracted great research interest. According to the active volcano diagram of different metals, a single metal features stronger or weaker binding energies toward a reaction intermediate, which makes it impossible to achieve the perfect combination of low overpotential and fast kinetics [88,89]. Therefore, the rational synergy between dual or multi-metals can not only effectively improve the electrical conductivity, but also modulate the electronic structure of active centers to optimize the adsorption energy, thus improving the electrocatalytic activity. Currently, the metal centers of common multi-metallic MOF catalysts are mainly based on transition metals, such as NiFe-MOFs, CoFe-MOFs, CoNi-MOFs, NiMn-MOFs, FeCoNi-MOFs, WCoFe-MOFs, CoNiMn-MOFs, FeCoMnNi-MOFs, and FeCoNiMnCu-MOFs [64,89–92].

Lan *et al.* [93] designed and synthesized a series of isomorphic MOFs (NNU-21-24) based on $Fe_2M(\mu_3\text{-}O)(CH_3COO)_6(H_2O)_3$ (Fe_2M, M = Fe, Co, Ni, Zn) clusters. The six CH_3COO^- groups in the clusters have been entirely replaced by COO^- of biphenyl-3,4′,5-tricarboxylic acid (H_2BPTC) ligands in NNU-21-24 (Figure 4a). Through structural optimization, NNU-23 showed the optimal OER activity with the overpotential of 365 mV at 10 mA cm^{-2}. According to both DFT calculations and experimental results, incorporating a second metal resulted in the d-band center close to the Fermi level, thus improving the OER performance. In 2020, Lou *et al.* [94] grew NiMn-based bimetallic MOF nanosheets on multi-channel carbon fibers (MCCF/NiMn-MOFs) and then used them as OER electrocatalysts. According to both DFT calculations and X-ray absorption fine structure (XAFS) spectroscopy, the strong interactions of the adjacent Ni and Mn sites in MCCF/NiMn-MOFs effectively promoted the proton coupling, resulting in the overpotential of 280 mV at 10 mA cm^{-2}. In addition, a novel CoCu-based bimetallic MOF nanobox (CoCu-MOF NB) was also synthesized *via* chemical etching reaction and successive cation and ligand exchange processes [63]. The LSV curves demonstrated that CoCu-MOF NBs required only a minimal overpotential of 271 mV for 10 mA cm^{-2}. Notably, Co-MOF NBs and Cu-MOF NBs have similar nanobox architectures and C_{dl} values, but CoCu-MOF has better OER performance, indicating that the synergistic effect between Co and Cu sites has a positive effect on promoting OER activity. Additional theoretical

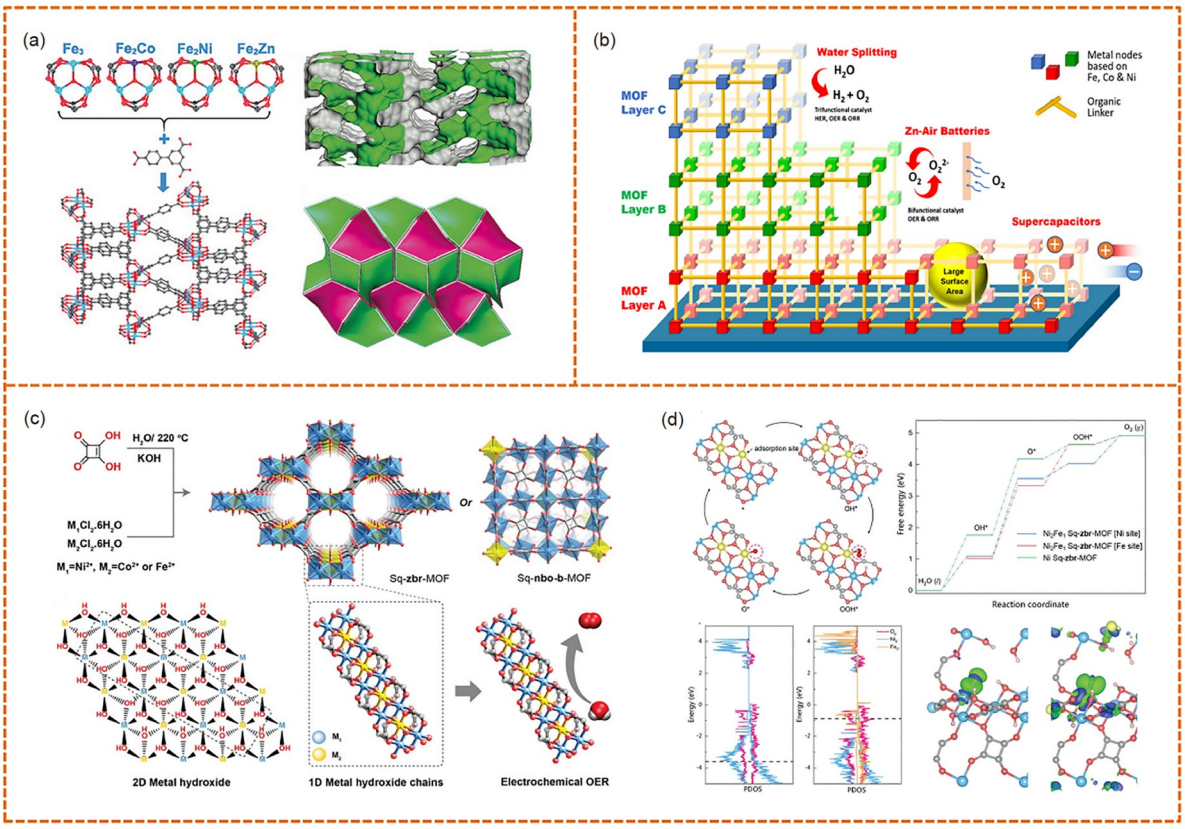

Figure 4 (a) Structural schematic diagrams of NNU-21–24. Reproduced with permission from Ref. [93], Copyright©2018 John Wiley & Sons, Inc. (b) Schematic illustration of trilayer Fe-Co-Ni MOF in electrochemical reactions. Reproduced with permission from Ref. [64], Copyright©2022 American Chemical Society. (c) Structural schematic diagrams of bimetallic Sq-MOFs. (d) DFT calculations of the samples for OER. Reproduced with permission from Ref. [95], Copyright©2022 John Wiley & Sons, Inc. (color online).

simulations revealed the effective regulation of the electronic structure of active sites was achieved by the strong electronic coupling between Co and adjacent Cu atoms, which substantially enhanced the overall reaction kinetics toward OER. In 2022, Mohamed Eddaoudi *et al*. [95] synthesized a series of chemically robust bimetallic squarate-based MOFs (Sq-MOFs) with **zbr** topology by adjusting the Ni^{2+} content in the bimetallic MOF system. Due to their open pore structure, strong affinity for water and catalytically capable one-dimensional metal hydroxide chains (Figure 4c), Sq-MOFs were considered as ideal candidates for OER catalysts. By testing catalysts with different metal ratios, it was demonstrated that Ni_3Fe_1 and Ni_2Fe_1 Sq-zbr-MOFs have superior OER electrocatalytic performance and good structural stability (Figure 4d).

The coupling effects among multiple metals in multi-metallic MOFs have been found to enhance the electronic occupancy status, leading to improved electrocatalytic activity compared with monometallic MOFs. Thus, more efforts have been made to develop an increasing number of multimetallic MOFs. In 2022, Mousavi *et al*. [64] reported a controllable reductive electrosynthesis method to *in-situ* grow a layer-by-layer assembled trimetallic Fe-Co-Ni MOF. The Fe, Co, and Ni MOF layers were arranged in an orderly and sequential manner, forming a trimetallic MOF stack (Figure 4b). Owning to the similarity towards ionic radius and electronegativities of different transition metals, Fe, Co, and Ni MOF layers have the same crystal structure. Additionally, Fe-Co-Ni MOF exhibited better electrochemical properties than monometallic Fe, Co, and Ni MOFs, bimetallic Fe-Co, Co-Fe, Fe-Ni, Ni-Fe, Co-Ni, and Ni-Co MOFs, indicating that the synergistic effect between Fe, Co, and Ni nodes had a positive effect on promoting OER activity.

3.3 Metal-doped MOFs

Recent studies have demonstrated that regulating the surface electrical structure of MOFs *via* metal doping is a highly effective method for enhancing their OER performance and stability. The doping of metals can enrich active sites, promote charge carrier migration, and optimize electrocatalytic kinetics. The similarity between metal-doped MOFs and multi-metallic MOFs is their ability to optimize the electronic structure of the metal active centers through the synergistic effect between metals, thereby improving the electrocatalytic performance. The metal-doped MOFs fea-

ture a low content of metal sites compared with the arbitrary ratio of multiple metals in multi-metallic MOFs, which usually have a positive contribution to the catalytic activity of the native metal sites in MOFs. In 2022, Jin *et al*. [73] prepared ultrathin MOF nanosheet array electrocatalysts doped with Y and Ce (NiYCe-MOF/NF) *via* a straightforward hydrothermal method, with Ni-MOF as the template. NiYCe-MOF/NF exhibited excellent OER performance and a small Tafel slope. Additionally, the electrochemical measurements of the samples showed that NiYCe-MOF/NF had a smaller polarization resistance due to the rich active catalytic sites and synergistic effects between different metal centers. Theoretical calculations and experimental results indicated that the doping of Y and Ce increased the electron transfer rate of Ni MOF/NF, resulting in excellent OER performance.

In 2022, an efficient electrocatalyst ($NiRu_{0.08}$-MOF) was constructed by optimizing the electronic structure of Ni-MOF with minor, atomically dispersed Ru [96]. The LSV curves demonstrated that Ni-MOF exhibited poor OER performance, requiring an overpotential of 252 mV to achieve a current density of 10 mA cm^{-2}. After a small amount of Ru atoms were doped into the Ni-MOF, the OER performance significantly improved. $NiRu_{0.08}$-MOF required only a minimal overpotential of 187 mV to achieve a current density of 10 mA cm^{-2}. The DFT calculation results indicated that Ru doping increased the conductivity and reduced the OER intermediate adsorption energy of $NiRu_{0.08}$-MOF, resulting in satisfactory OER electrocatalytic activity. Drawing inspiration from the desirable features of 3D hollow spherical NiCo-MOFs and the high OER activity of Ru, Du *et al*. [97] developed an innovative electrocatalyst based on Ru-doped NiCo-MOF hollow porous nanospheres (Ru@NiCo-MOF HPNs). In this catalyst, Ni, Co, and O were homogeneously dispersed across the bulk of the hollow nanospheres, while Ru was uniformly distributed over the shell. Taking advantage of the high porosity and large surface area of MOFs and the optimized electronic properties resulting from Ru doping, the Ru@NiCo-MOF HPNs demonstrated superior water oxidation performance, with an overpotential of only 284 mV at 10 mA cm^{-2} in 1.0 M KOH, as well as a small Tafel slope of 78.8 mV dec^{-1}. The experimental results indicated that the ultra-low amount of Ru not only increased the active surface area of the catalyst but also modified the electronic structure of Ni and Co, resulting in superior OER performance. Yang *et al*. [74] designed and fabricated a vanadium-doped nickel organic framework (V_{1-x}-Ni_xMOF) array on nickel foam (NF) using a facile two-step solvothermal method. The OER activity of V_{1-x}-Ni_xMOF was significantly improved by doping V, showing better performance than corresponding single metallic Ni-MOF, NiV-MOF, and RuO_2 catalysts at high current density (>400 mA cm^{-2}). The experimental results indicated that the V doping not only offered more efficient catalytic active sites for the OER process but also adjusted the binding energy between the active sites and the intermediates, resulting in an outstanding OER activity and excellent stability of V_{1-x}-Ni_xMOF in the alkaline electrolyte.

3.4 Composite MOFs

The integration of different functional materials with MOFs can synergistically exploit their respective advantages and avoid their disadvantages, endowing the composites with rich pore structures, large specific surface areas, excellent electrical conductivity, and rich active sites, thereby improving the electrocatalytic performance. Notably, the formation of heterostructures in composites can also generate highly reactive surfaces/interfaces between two different phases, thereby inducing lattice distortion or unsaturated defective active sites and further enhancing the electrocatalytic activity [98–101]. Therefore, numerous functional materials, such as metal oxides/hydroxides, carbon materials, and noble metal materials, are being used to composite with MOF materials to enhance their electrocatalytic performance.

Metal oxide/hydroxide nanomaterials have been extensively studied and shown promising results due to their low cost and excellent redox capability. Embedding them with MOFs could achieve further improvement in their physicochemical properties. For example, Zhou *et al*. [98] utilized the lattice of a monolayered Co-based MOF to embed $CoFeO_x$ nanoparticles (Figure 5a), creating highly active sites at the interfaces between two phases. According to structural characterization and analysis, compared with the CoN_4 site, interface Co exhibited higher valence states and electronic configurations, which resulted in higher OER activity (Figure 5b, c). In 2022, Li *et al*. [69] fabricated Fe-doped-(Ni-MOFs)/FeOOH by Fe doping and interfacial FeOOH engineering. Based on the advantages of the formation of Fe−O−Ni−O−Fe bonding, Fe-doped-(Ni-MOFs)/FeOOH exhibited excellent OER electrocatalytic activity and the overpotential of only 210 mV at 15 mA cm^{-2}. The theoretical calculations showed that the Fe-doped-(Ni-MOFs)/FeOOH was doubly regulated through Fe doping and interfacial FeOOH effect *via* Fe−O−Ni−O−Fe bonding, which delivered a moderate but relatively stronger oxygen binding strength (E_{OH}^{*} = −0.32 eV and E_{O}^{*} = −0.01 eV), optimizing the adsorption/desorption process of oxygen intermediates during OER, resulting in lower overpotential and small Tafel slope.

Integrating noble metal with MOFs can lead to MOFs with more exposed metal sites and an enriched electron environment, which can effectively improve the electrocatalytic performance. Qiao *et al*. [102] demonstrated an interfacial-bond-induced modulation of reaction intermediates for ac-

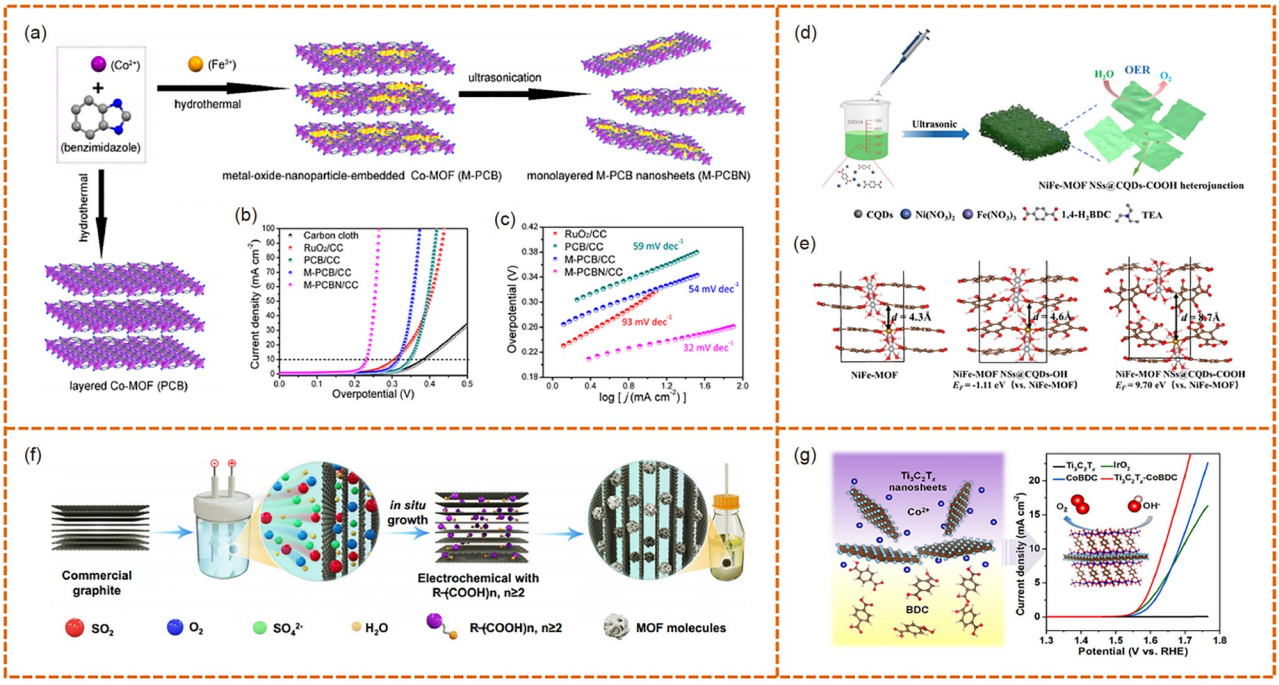

Figure 5 (a) Synthesis procedure of catalysts. (b) LSV curves and (c) corresponding Tafel plots of M-PCBN/CC and control samples. Reproduced with permission from Ref. [98], Copyright©2020 American Chemical Society. (d) Strategy for constructing NiFe-MOF NSs@CQDs-COOH. (e) Structural schematic diagrams and calculation analysis of samples. Reproduced with permission from Ref. [103], Copyright©2022 Elsevier. (f) Schematic illustration of the synthesis process of NiFe-MOF//G. Reproduced with permission from Ref. [52], Copyright©2022 Springer Nature. (g) Scheme for the synthesis of $Ti_3C_2T_x$-CoBDC, and LSV curves of samples. Reproduced with permission from Ref. [47], Copyright©2017 American Chemical Society (color online).

celerated OER by creating a heterostructure of Pt nanocrystal and 2D (two-dimensional) nickel MOFs (Pt-NC/Ni-MOF). In the heterostructure of Pt-NC/Ni-MOF, the 2D Ni-MOF and Pt-NC were chemically coupled in an atomically matched mode to lead to a distinctive interface with Ni−O−Pt bonds, which resulted in charge relocation. This charge relocation in turn gave rise to an increased electron density for Pt and a high-energy Ni 3d state of Ni-MOF, thus promoting the OER reaction. Carbon materials have been considered excellent conductive substrates and highly dispersible carriers. Combining MOF with carbon materials is expected to further enhance the electrical conductivity and catalytic activity of the material. In 2022, Wang *et al*. [103] employed a one-step "bottom-up" synthesis strategy at room temperature, using carboxylated carbon quantum dots (CQDs-COOH) to induce the *in-situ* formation of 2D NiFe-MOF NSs (Figure 5d). Based on DFT calculations, it has been confirmed that the layer spacing of NiFe-MOF was enlarged by the introduction of CQDs-COOH (Figure 5e). Additionally, CQDs-COOH enhanced the positive charge on the active sites, thereby improving the OER activity of NiFe-MOF. The optimized catalyst showed amazing OER performance with an overpotential of 261 mV at 10 mA cm^{-2} and a very small Tafel slope of 56 mV dec^{-1}. Hou *et al*. [52] proposed a strategy to improve the OER activity of low-conductivity NiFe-MOFs by confining them between multilayered graphene sheets (NiFe-BTC//G) (Figure 5f). The NiFe-BTC//G exhibited a remarkable OER performance, with a record-low overpotential of 106 mV to achieve 10 mA cm^{-2}, and maintained its activity for over 150 h. This was in stark contrast to the pristine NiFe-BTC, which needed an overpotential of 399 mV at the same current density. Additionally, the DFT calculation and XAFS confirmed that the nanoconfinement provided by graphene multilayers not only created highly reactive NiO_6-FeO_5 distorted octahedral species in the MOF structure but also reduced the limiting potential for the water oxidation reaction.

MXenes, as an emerging material, possess high electroconductivity, hydrophilicity, and excellent stability. In addition, thanks to the ultra-low work function and electronegative surface, it can modulate the electrophilicity of the active sites to improve the catalytic performance of the multicomponent catalyst. Based on this, Huang *et al*. [47] prepared a new MXene-MOF composite ($Ti_3C_2T_x$-CoBDC) by an interdiffusion reaction. CoBDC was perfectly affixed to the surface of $Ti_3C_2T_x$ nanosheets. The resulting composite exhibited excellent OER electrocatalytic activity (Figure 5g).

3.5 Conductive MOFs

Although the traditional MOFs have been widely applied in OER, they mostly exhibit insulation and low conductivity,

which significantly limits their availability in OER. The 2D conductive MOFs (2D *c*-MOFs), as an emerging crystalline material composed of metal nodes and conjugated organic linkers, can provide great scopes for constructing high-performance MOF-based OER electrocatalysts. Their conductive mechanisms include hopping, through-space, and through-bond mechanisms (Figure 6a) [104]. To date, tremendous efforts have been devoted to the synthesis and characterization of new MOFs with excellent electrical conductivity, while a large number of theoretical studies have confirmed the potential of 2D *c*-MOFs for OER applications (Figure 7) [105,106]. This class of material inherits the advantages of traditional MOFs, such as high specific surface area, versatile structures, high porosity, and abundant exposed active sites, which endows them with great potential in OER. Particularly, the hybrid of frontier orbits of conjugated ligands and d-orbits of the transition metals featured a strong d-π interaction, which promotes the delocalization of electrons in the 2D plane, thereby endowing them with a narrow bandgap and high intrinsic electrical conductivity. Furthermore, the structures and electronic features of MOF catalysts can be regulated *via* a rational design strategy at the molecular and atomic levels based on demands [104,107]. The design of high-performance 2D *c*-MOF electrocatalysts accounted for several key factors, mainly including active metal sites, conductivity, and porous architectures.

The metal nodes have been proven as the dominant active centers and are directly related to the intrinsic activity of the 2D *c*-MOFs as OER electrocatalysts, which promotes the generation/conversion of intermediates (OH^*, OOH^*, and O^*) and charge transfer during the OER process. Hence, immobilization of transition metals into the backbone of 2D *c*-MOFs has been widely regarded as a general strategy to

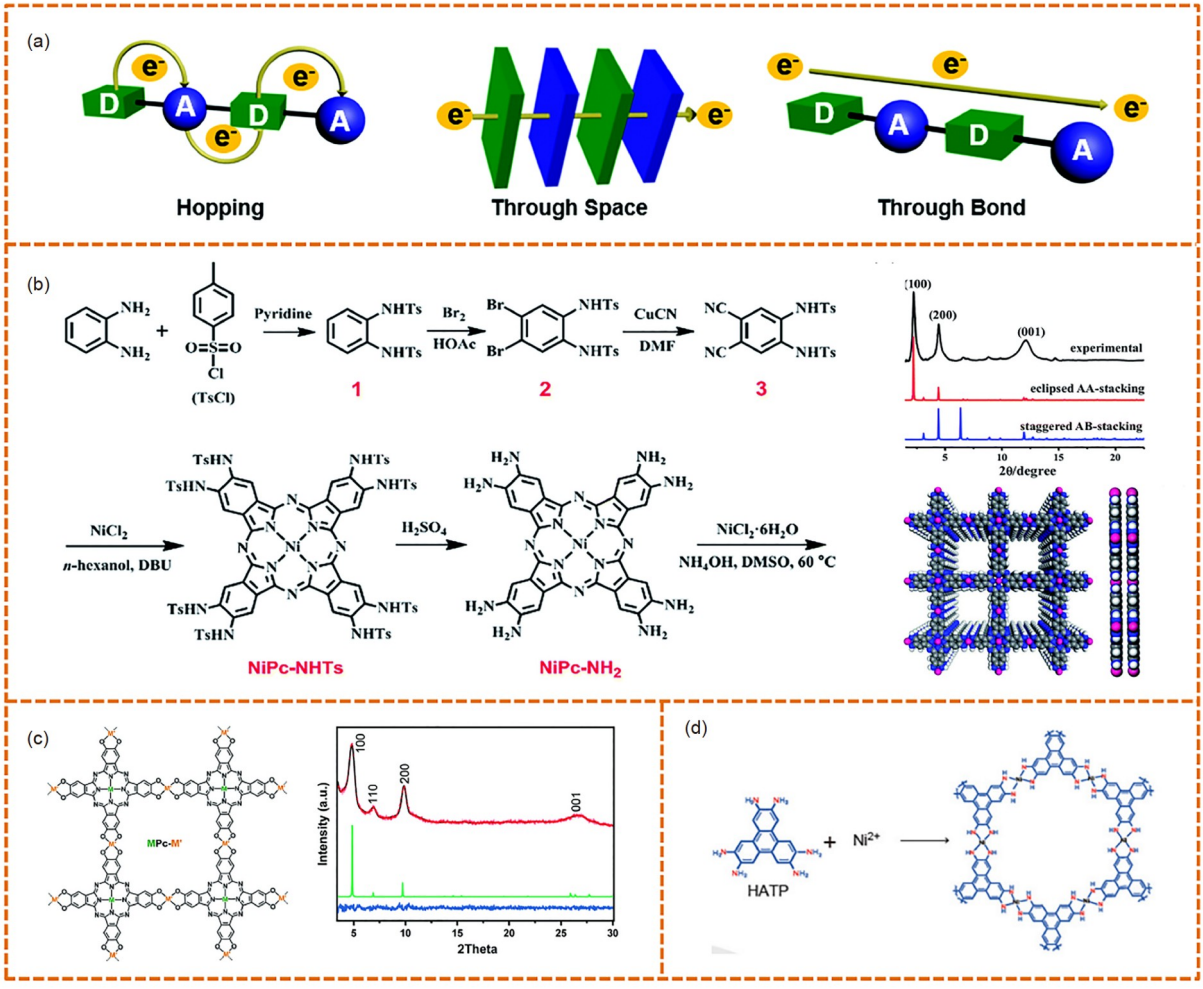

Figure 6 (a) Schematic illustration of charge transport in 2D *c*-MOFs. Reproduced with permission from Ref. [104], Copyright©2018 Royal Society of Chemistry. (b) Scheme for the synthesis of NiPc-MOF and its structural schematic diagrams. Reproduced with permission from Ref. [108], Copyright©2018 Royal Society of Chemistry. (c) The chemical structure and PXRD pattern of MPc-M'. Reproduced with permission from Ref. [109], Copyright©2021 Royal Society of Chemistry. (d) Strategy for constructing 2D $Ni_3(HITP)_2$. Reproduced with permission from Ref. [110], Copyright©2020 American Chemical Society (color online).

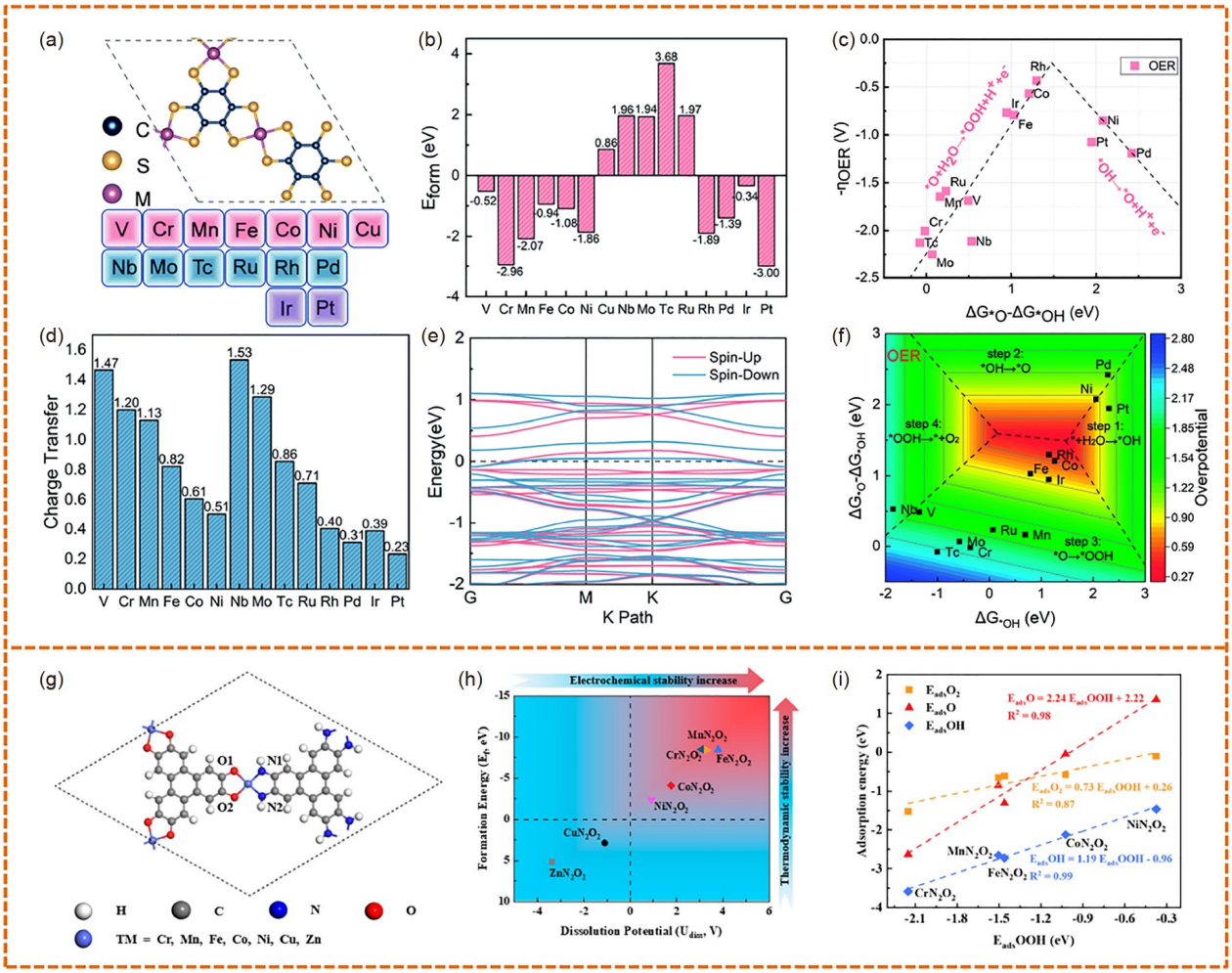

Figure 7 (a) Structure models, (b) the formation energy, and (c) the volcano plot of $M_3(C_6S_6)_2$. (d) Charge transfer between C_6S_6 and metals. (e) Calculated band structure of $Rh_3(C_6S_6)_2$. (f) The contour map of OER activity tendency on $M_3(C_6S_6)_2$. Reproduced with permission from Ref. [105], Copyright©2022 Royal Society of Chemistry. (g) Structural schematic graphs of 2D MOFs TMN_2O_2. (h) Formation energy of TMN_2O_2 and corresponding U_{diss} of metal atoms. (i) Adsorption energy of different intermediates on TMN_2O_2. Reproduced with permission from Ref. [106], Copyright©2022 American Chemical Society (color online).

construct OER electrocatalysts with high utilization of catalytic sites. Recent demonstrations of this design strategy were reported in a series of 2D *c*-MOFs with diverse 3d transition metal sites, including MO_4 and MN_4 (M: Fe, Co, Ni, Cu, Mn, *etc*). For example, Du *et al*. [108] synthesized a 2D *c*-MOF composed of 2,3,9,10,16,17,23,24-*octa*-aminophthalocyaninato nickel-(II) and $NiCl_2{\cdot}6H_2O$ (NiPc-MOF) (Figure 6b). The NiPc-MOF film with NiN_4 sites on fluorine-doped tin oxide (FTO) showed prominent OER activity with an overpotential of 350 mV and a Tafel slope of 74 mV dec^{-1}, as well as stability over 50 h in alkaline electrolytes. The $Co_3(HITP)_2$ (HITP = 2,3,6,7,10,11-hexaiminotriphenylene) with high loading of Co-N_4 sites (23.44 wt% of Co element) was also investigated for OER [111]. The as-prepared $Co_3(HITP)_2$ exhibited an electrical conductivity of 1,150 S m^{-1} at 300 K. By combining the experimental and DFT theoretical calculation, it was verified that the synergistic effects of high conductivity, porous structure, and the high loading of active Co-N_4 sites resulted in an excellent catalytic activity with an overpotential of 254 mV at 10 mA cm^{-2} and a Tafel slope of 86.5 mV dec^{-1}.

For 2D *c*-MOFs, the regulation of electronic structure at the molecular or atomic level by tailoring the organic ligand and metal types makes them possess high inherent catalytic activity and selectivity. In this regard, introducing the extra metal atoms and varying the substitutional groups of the ligands were employed as two main strategies to modulate the electronic structure. To date, a series of 2D *c*-MOFs with distinct coordination environments of metal active sites have been exploited for electrocatalytic OER, and the crucial role of different metal centers was also illustrated. For example, Song *et al*. [112] successfully achieved a series of bimetallic conductive MOFs (denoted as NiPc-$NiFe_x$) by replacing sectional Ni-O_4 sites with Fe-O_4 sites. Owing to the elec-

tronic interaction between Ni and Fe sites, the optimal NiPc-$NiFe_{0.09}$ showed remarkable OER performance with an overpotential of 300 mV at 10 mA cm^{-2} and an excellent TOF value of 1.943 s^{-1}. Additionally, the incorporation of highly conjugated ligands in 2D *c*-MOFs can also effectively optimize the electronic structure of active sites and improve catalytic performance. For example, an NiPc-Ni with NiN_4 and NiO_4 sites has been demonstrated as an effective OER catalyst with enhanced OER performance [109]. It was revealed that the synergistic interactions of bimetallic sites modulated the electronic structure of the active centers, while the d-band center was nearer to the Fermi level, thereby enhancing the binding ability of oxygen intermediates (OH^*, OOH^*, and O^*) and promoting the intrinsic OER activity. The prepared NiPc-Ni exhibited higher OER performance with a low onset overpotential and a Tafel slope of 83 mV dec^{-1} (Figure 6c).

In addition to the vital role of metal nodes, the architectures (including pore structure, morphology, and thickness) of 2D *c*-MOFs significantly affect the OER catalytic activity as well [113]. Wang *et al*. [110] prepared a 3-layer $Ni_3(HITP)_2$ film electrode with good OER performance (Figure 6d). It was revealed that the OER performance of $Ni_3(HITP)_2$ film was dependent on the layer of this film on the electrode. The research in this area is currently very limited and a great deal of work should be invested in revealing the influence of the above characteristics on the OER properties. In parallel, the corresponding relationships between structure and properties should also be discovered to optimize the construction strategy of 2D *c*-MOF electrocatalysts with excellent OER activity.

3.6 Substrate-grown MOFs

Currently, most prepared MOF catalysts usually acted as nanoscale powder samples, which are immobilized on glassy carbon electrodes with a binder before electrocatalytic tests. However, the partial active catalyst sites of electrodes prepared *via* this method can be covered, and the use of binder also increased the internal charge transfer resistance. In addition, the persistent generation of bubbles can affect catalyst adhesion toward the electrode surface in the OER test, leading to partial detachment and potentially affecting the catalyst performance [114,115]. Therefore, selecting suitable conductive substrates for the *in-situ* growth of MOFs is highly desirable. The conductive substrates can significantly enhance the conductivity of catalysts and enable faster kinetics. The array structure of MOFs obtained by *in-situ* growth can achieve a high-density dispersion of catalysts and facilitate the exposure of active sites. Recently, conductive substrates represented by NF have been widely investigated due to their significant advantages in providing conductive pathways, catalyst carrying, bubble aggregation drainage, mechanical stability, and positive synergistic effects between electrocatalysts and substrates [78]. Moreover, the properties exhibited by such MOF complexes grown on substrates make them one of the most promising materials to meet industrialization requirements.

Zhao *et al*. [26] demonstrated a general chemical deposition method to prepare ultrathin MOF nanosheet arrays with different metal-oxygen units (MO_6 units; M = Ni, Fe or Cu), using NF as a self-supporting substrate (Figure 8a, b). The nanoarrays exhibited excellent electrocatalytic OER activity with a low overpotential of 240 mV at 10 mA cm^{-2} and negligible activity decay over 20,000 s of stable operation (Figure 8c). Lin *et al*. [114] showed an innovative approach for synthesizing a 3D electrode using a self-templating route, whereby MIL-53(FeNi) nanosheets were grown on the surface of NF *via* a one-step solvothermal method. The prepared MIL53(FeNi)/NF electrode exhibited excellent OER performance with an overpotential of 233 mV at 50 mA cm^{-2}, a mass activity of 19.02 A g^{-1}, and a Tafel slope of 31.3 mV dec^{-1}, which was attributed to the advantages of the *in-situ* growth method. DFT calculations and experiments confirmed that the introduction of Fe enhanced the electrochemically active sites of the MIL-53, accelerated electron transfer, and regulated the electronic structure of active sites, thereby improving the intrinsic activity. Lu *et al*. [78] developed an efficient and durable bifunctional electrocatalyst by *in-situ* growing homogeneously mixed and distributed Fe- and Ni-MOFs on NF (MFN-MOFs) using a simple one-step solvothermal strategy. The as-prepared materials exhibited inter-molecular synergistic interactions, which not only facilitated the vital charge transfer process of redox reactions but also achieved a high dispersion of the active metal sites, thus increasing the active site density and achieving outstanding OER performance. In addition, the binder-free also greatly enhanced the mechanical adhesion and effective bonding between MOF and NF, endowing the optimized MFN-MOF (2:1)/NF electrode with excellent OER performance. The Cu foam (CF) was also used as a conductive substrate for the direct growth of MOFs. Gu *et al*. [116] have developed a liquid-phase epitaxial layer-by-layer growth approach to produce oriented thin films of 3D MOF Co/Ni$(BDC)_2$TED (TED = triethylenediamine) nanosheet arrays on CF. The Co/Ni$(BDC)_2$TED thin film electrode was found to exhibit high activity for the OER, and the OER activity can be further improved by adjusting the thicknesses and Co/Ni ratios. DFT calculations have shown that the enhanced electrocatalytic activity was attributed to the synergistic effect of Co/Ni and the abundance metal sites. Growing MOFs *in-situ* on hydrophobic carbon substrates such as graphite foam (GF), carbon cloth, and carbon paper was also considered an effective strategy to enhance OER performance. Feng *et al*. [117] utilized a hydrothermal method to synthesize an efficient OER electrocatalyst by *in-*

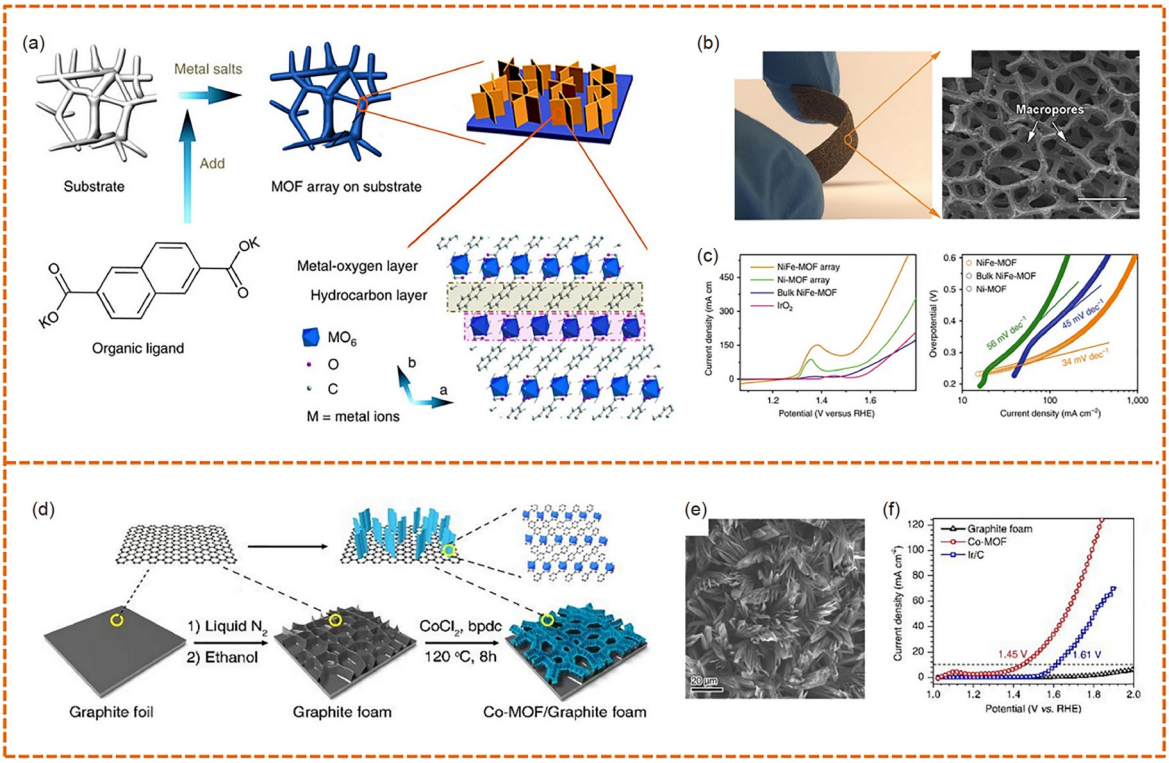

Figure 8 (a) Scheme of the synthesis and structural model NiFe-MOF nanosheet array on the substrate. (b) The optical image and SEM image of NiFe-MOF electrodes. (c) LSV curves and corresponding Tafel plots of samples. Reproduced with permission from Ref. [26], Copyright©2017 Springer Nature. (d) Schematic illustration for the synthesis procedure of the Co-MOF/Graphite foam. (e) SEM image of the Co-MOF/GF. (f) LSV curves of Co-MOF/GF and control samples. Reproduced with permission from Ref. [117], Copyright©2018 John Wiley & Sons, Inc. (color online).

situ growing $Co(bpdc)(H_2O)_4$ (Co-MOF, H_2bpdc = biphenyl-4,4′-dicarboxylic acid) arrays on a three-dimensional GF (Figure 8d, e). The obtained Co MOF/GF exhibited a low overpotential, approximately 220 mV at 10 mA cm^{-2}. The experiment also showed that the CoOOH nanosheets *in-situ* obtained from the Co-MOF were essential to drive the OER process (Figure 8f).

3.7 Amorphous MOFs

In addition to the regulation of the morphological structure and compositions, tailoring the crystallinity of catalysts *via* the optimization of preparation methods is also vital for improving their electrocatalytic performance. A variation in crystallinity can affect the lattice-ordered structure and atomic arrangement, leading to an increase in the external active sites of the catalyst and conductivity. Generally, MOFs exhibit ordered atomic arrangement and high crystallinity, which might result in sluggish electron transfer and exposed active sites, hindering their electrocatalytic OER activity to some extent [118,119]. Conversely, amorphous MOFs are characterized by diverse morphology, rich pores, numerous active sites, and high conductivity, which provides new opportunities for improving the OER activities of MOF electrocatalysts.

It is shown that the crystallinity of MOF materials can be effectively modified by tuning the species and ratios of metal combinations. Mai *et al.* [120] presented a simple approach for synthesizing low-crystalline bimetallic MOF nanoparticles (Fe_xNi_y-BDC) *via* regulation of the coprecipitation process between Fe/Ni ions and BDC^{2-}. The monometallic Fe-BDC exhibited high crystallinity, while the crystallinity of Fe_xNi_y-BDC deteriorated as the Fe/Ni ratio decreased. The LSV curves demonstrated that Fe_1Ni_2-BDC required only a minimal overpotential of 260 mV at 10 mA cm^{-2}. In addition, Fe_1Ni_2-BDC exhibited the highest TOF value, it was indicated that introducing an appropriate proportion of Ni^{2+} into Fe-BDC can obtain highly active sites. According to both experimental and theoretical analysis, the low-crystalline Fe_1Ni_2-BDC showed better catalytic OER performance mainly benefiting from its abundant active sites, faster charge transfer, and enhanced reaction kinetics. Huang *et al.* [121] have achieved the transition from a crystalline to an amorphous state of Co_xFe_yMOFs by tuning the ratio of Co/Fe to coordinate with the H_2BDC. According to DFT calculations, it was found that the defect formation energies of Co_xFe_y-MOFs decreased significantly with the reduction in the Co/Fe ratio, resulting in the formation of long-range

disordered structures and a large number of defects within the MOFs. This structure allowed the bimetallic Co_xFe_y-MOFs abundant active sites and fast charge transfer. In addition, introducing Fe ions into Co-MOF can adjust the electronic structure of Co sites, which promoted the adsorption/desorption of OER oxygen-containing intermediates, thereby improving the electrocatalytic performance of OER.

Also, amorphous structures can be obtained by external physical stimulation. In 2022, Wang *et al*. [122] transformed the crystalline material Co-MOF into the amorphous material Fe@Co-MOF by grinding, exfoliating, and doping Fe. This process effectively modulated the electronic structure of the metal active sites, resulting in excellent electrocatalytic performance. Controllable preparation of crystalline transformation of Co-MOF was achieved by varying the amount of Fe doping, which produced an amorphous structure with adequate defects Fe@Co-MOF-3. The introduction of lattice distortion and interface results in a significant improvement in the catalytic activity of Co-MOF, which exhibited an ultralow overpotential of 248 mV for OER at a current density of 50 mA cm^{-2}. In 2022, Meng *et al*. [123] synthesized a series of highly efficient and stable $Fe_x(NiCu)_{3-x}$-MOF catalysts for the OER using an ultrasonic method. The prepared ternary $Fe_x(NiCu)_{3-x}$-MOFs exhibited an amorphous structure with more exposed active sites and rapid charge transfer. The optimal FeNiCu-MOF catalyst has an overpotential of only 260 mV at 10 mA cm^{-2}. The outstanding performance was due to the amorphous MOF structure and the synergistic effect of the multi-metal sites. Furthermore, DFT calculations demonstrated that the Fe sites of the FeNiCu-MOF played a vital role during the OER process.

3.8 2D MOFs

The reduction of catalyst sizes and the preparation of ultrathin 2D materials are considered keys for achieving high catalytic performance. Most MOFs feature limited mass transport, poor electrical conductivity, and low density of metal active sites. 2D MOF nanosheets have received increasing research attention owing to their ultrathin thickness and large surface areas [107]. Similar to amorphous MOFs containing richer active sites, 2D MOF nanosheets not only provide abundant active sites, but also exhibit fast mass and electron transfer. In addition, owing to high mechanical flexibility and optical transparency, ultrathin 2D MOFs have been considered a promising alternative for developing flexible electronic devices [124].

For example, Tang *et al*. [46] successfully synthesized ultrathin 2D bimetal-organic framework nanosheets (NiCo-UMOFNs) with coordinatively unsaturated metal sites using a facile ultrasonic method at room temperature. NiCo-UMOFNs possessed a uniform thickness of approximately 3.1 nm, which corresponded to either four metal coordination layers or three coordination structural layers (2.9 nm). When loaded onto copper foam, the NiCo-UMOFNs catalyst displayed remarkable OER activity with a very small overpotential of 189 mV at 10 mA cm^{-2} under alkaline conditions. The ultrathin 2D nanosheets generated numerous coordination unsaturated active sites, which can serve as active centers to enhance the OER activity. Additionally, the coupling effect between Co and Ni further enhanced the electrocatalytic OER performance. In addition, a bottom-up solvothermal method was employed to synthesize heterometallic Ni-M-MOF (M = Fe, Al, Co, Mn, Zn, and Cd) nanosheets with a thickness of only a few atomic layers (Figure 9a) [125]. The ultrathin MOF nanosheets were directly utilized as efficient electrocatalysts for OER, exhibiting a low overpotential of 221 mV at 10 mA cm^{-2} and a small Tafel slope of 56.0 mV dec^{-1}. Additionally, they exhibited excellent stability, maintaining their activity without any noticeable decay for at least 20 h.

He *et al*. [126] successfully synthesized a series of $(Fe(II)_1Fe(III)_1)_x$/NMOF-Co electrocatalysts with controllable molar ratios. The atomic force microscopy (AFM) measurements revealed that the thickness of nanosheets was approximately 4.0 nm. Notably, the 2D $(Fe(II)_1Fe(III)_1)_{0.6}$/NMOF-Co exhibited outstanding OER performance, displaying an overpotential of 297 mV at 10 mA cm^{-2}, which was significantly worse than that of $(Fe(II)_1Fe(III)_1)_{0.6}$/Bulk-MOF-Co. The experimental results indicated that the $(Fe(II)_1Fe(III)_1)_x$/NMOF-Co provided abundant active sites to enhance the electron transfer rate, leading to the improvement of catalytic performance. Wang *et al*. [127] synthesized NiFe-bimetal 2D ultrathin MOFs nanosheets (NiFe-UMNs) using a simple ultrasonic oscillation method. The thickness of NiFe-UMNs was approximately 10 nm, corresponding to ten coordination layers, indicating their ultrathin feature. The NiFe-UMNs exhibited satisfactory OER electrocatalytic performance with an onset potential of 1.450 V (*vs*. RHE) and an overpotential of 260 mV at 10 mA cm^{-2}. The high catalytic activity was attributed to the fact that 2D structures can expose richly active sites and give a synergistic effect between the bimetallic Ni and Fe.

Generally, a single strategy often fails to achieve the desired catalytic performance. Hence, multiple strategies are often utilized in the hope of simultaneously achieving multidimensional modulation of material conductivity, active site density, and active site electronic structure, thereby achieving satisfactory OER activity. For example, Ma *et al*. [128] introduced a new method to immobilize pepsin (PEP) on zeolitic imidazolate framework-8 (ZIF-8) *via* surface modification. ZIF-8 can coordinate with Ni^{2+} *via* electrostatic interaction, thereby changing the inherent hydrophobicity of ZIF-8 (Figure 9b). In addition, the immobilization of PEP on ZIF-8 is also favorable for enhancing its stability and maintaining its excellent con-

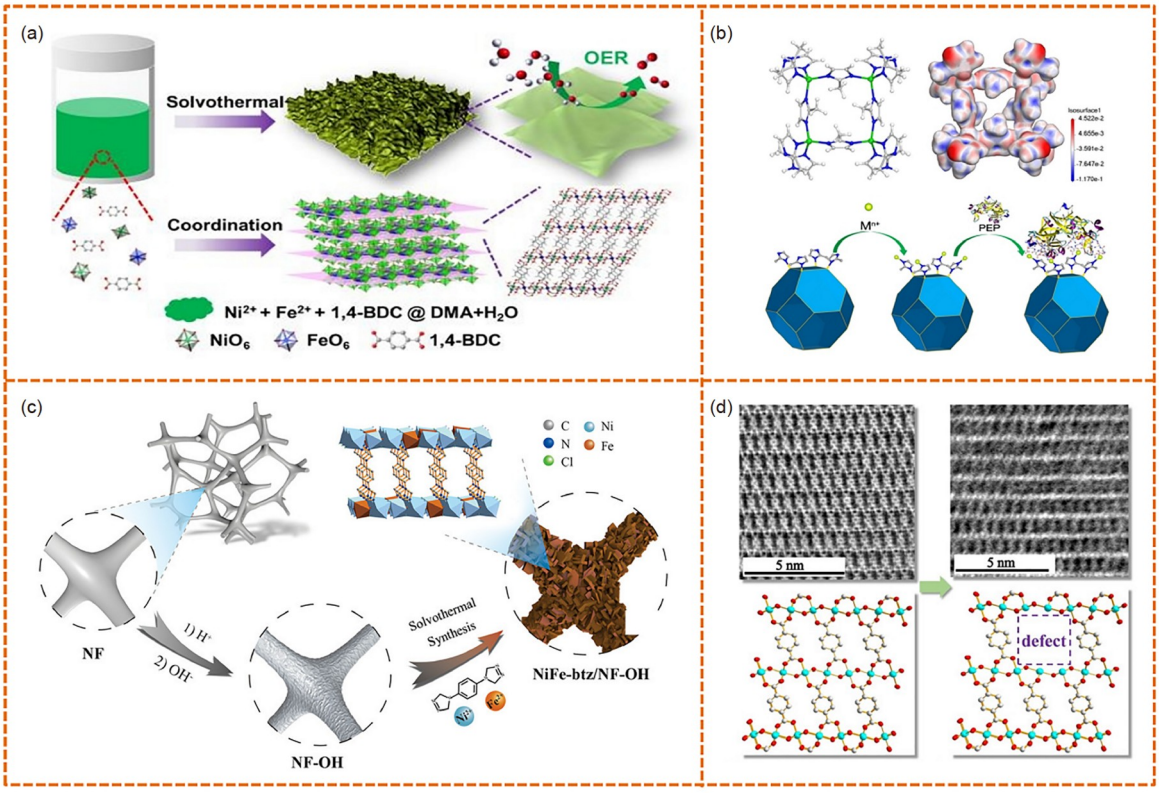

Figure 9 (a) The synthesis strategy of Ni-Fe-MOF NSs. Reproduced with permission from Ref. [125], Copyright©2019 John Wiley & Sons, Inc. (b) Schematic diagrams of structure and synthesis procedure of ZIF-8@PEP-M. Reproduced with permission from Ref. [128], Copyright©2022 John Wiley & Sons, Inc. (c) Schematic illustration for the synthesis procedure of the NiFe-btz/NF-OH. Reproduced with permission from Ref. [67], Copyright©2022 John Wiley & Sons, Inc. (d) iDPC-STEM images and structure modes of samples. Reproduced with permission from Ref. [72], Copyright©2022 John Wiley & Sons, Inc. (color online).

ductivity and electrochemical properties. As a result, ZIF-8@PEP-Ni exhibited excellent OER performance in neutral aqueous solutions. Zhu *et al*. [67] prepared a class of ionic bimetallic MOF films as OER catalysts, which featured an overpotential of 239 mV at a current density of 10 mA cm^{-2} (Figure 9c). The excellent electrocatalytic performance of the OER catalyst was mainly attributed to the following aspects: the NF substrate with high electrical conductivity improved the overall electrical conductivity of the material and the contact area between the catalyst and the electrolyte; the synergistic effect between Ni and Fe bimetals enhanced the catalytic capacity of the active sites, and the positive effect of Cl^- ion on the charge density near the Fermi energy level. In 2022, Zhao *et al*. [72] prepared a series of mixed metal and ligand multivariate MOFs (MTV-MOFs). The presence of mixed ligands resulted in uniform lattice strain, which weakened some of the coordination bonds in the prepared materials (Figure 9d). These coordination bonds can be selectively split through moderate heat treatment, resulting in ligand-unsaturated metal sites, conductive Ni@C, and multilevel pore structures, which are favorable for electrocatalytic OER processes. This phenomenon was precisely analyzed *via* low-dose integrated differential phase contrast scanning transmission electron microscopy (iDPC-STEM) technique.

4 Structural reconstruction of MOFs

The well-defined structure and active center are vital for elucidating the catalytic mechanism of OER catalysts, and the clarification of catalytic mechanisms can also be fed back to the directed construction of targeted catalysts. Previous extensive reports have confirmed that the partial or complete reconstruction of conventional inorganic catalysts occurred *in-situ* on the surface during OER to form metal oxides or hydroxides layer as the true reactive sites [129–131]. For MOF-based OER electrocatalysts, in which the coordination bonds feature weaker stability than the ionic bonds in inorganic materials, partial or complete structural reconstruction of MOF-based catalysts may also be inevitable in the test environment (pH 13, 14) [24,132]. In most previous studies, researchers only simply assumed that the MOF materials could remain stable in the OER test environment,

thus the pristine MOF was regarded as the catalytically active phase. However, this viewpoint is actually unreasonable. Although certain MOFs can maintain a degree of stability in alkaline solutions, the chemical stability of a catalyst does not guarantee its electrochemical stability. Notably, most transition metal-based (Fe, Co, Ni, and Cu) materials used as OER catalysts feature redox potentials around the theoretical voltage of OER, and variations in metal valence states accompanying the OER process also affect the coordination environment of metal nodes, resulting in the change of the initial structure [50]. In addition, since the structural reconstruction process of the MOFs can occur after immersing the electrolyte and before the occurrence of OER, and the reconstruction does not necessarily cause significant changes in the morphology of the pristine MOFs, it is also debatable to determine the stability of catalysts only from a single aspect such as stability curves and morphological characteristics before and after cycling.

Regarding the above analysis, numerous researchers have assumed that most OER catalyst-based MOF, particularly carboxylic acid-based MOF and imidazole-based ZIF materials with excellent OER electrocatalytic activities, will undergo partially/completely structural reconstruction in the experimental environment or during the reaction process. Moreover, more than one structural reconstruction process may occur, resulting in the generation of metal hydroxides/hydroxyl oxides with high catalytic activity. Therefore, such unstable MOFs are usually considered as pre-catalysts rather than true catalysts [49,133,134]. In addition, the structural properties (topology, porosity, size, composition, *etc.*) of such MOF catalysts can affect the reconstruction process, thereby triggering changes in the active species and the catalytic activity [135]. In this section, we focused on four aspects of MOF-based OER catalysts, including partial reconstruction, complete reconstruction, reconstruction effects, and reconstruction strategies, to discuss their catalytically active phases and catalytic mechanisms in detail.

4.1 Partial reconstruction

Similar to inorganic catalysts, some MOF-based catalysts underwent partial surface reconstruction in the OER test environment owing to the formation of amorphous metal hydroxide films on the surface of large-size MOF materials after self-reconstruction, which can protect the internal MOFs structure [136,137]. Thus, a heterogeneous structure would be formed and the synergistic effect of the two components could enhance the catalytic efficiency of OER. Chen *et al*. [138] prepared two samples of dehydrated Ni-BDC-3 and hydrated Ni-BDC-1 with the presence of weak hydrogen bonds generated by coordinated water molecules, respectively (Figure 10a). Both MOFs were first activated as pre-catalysts by electrochemical cyclic voltammetry (CV). It was found that the dehydrated Ni-BDC-3 was rapidly and completely reconstructed to NiOOH. In contrast, the weak hydrogen bonding in the hydrated Ni-BDC-1 had a significant inhibitory effect on its structural reconstruction, which led to a partial phase transition of Ni-BDC-1 to obtain a heterojunction structure of NiOOH and MOF. The MOF heterojunction obtained an ultra-low overpotential of 225 mV at a current density of 10 mA cm^{-2}, which was significantly superior to the single-phase NiOOH (332 mV) obtained after complete reconstruction by Ni-BDC-3. Theoretical calculations confirmed that a strong planar electrostatic potential was established between the internal structure of MOF and the surface self-reconstructed NiOOH. This suggested that the pristine MOF structure could serve as an electron-absorbing trimmer to modulate the electronic configuration of the Ni active sites, thus degrading the reaction energy barrier of the OER.

Our group prepared Fe-MOF octahedra and Ni-MOF nanosheets with positive and negative surface charges, respectively. Benefiting from the differences in the morphological properties and surface charges of Fe-MOF and Ni-MOF, FeNi-based MOF composites based on two types of metals can be obtained *via* simple sonication, which reached an overpotential of only 275 mV at a current density of 10 mA cm^{-2} without significant property degradation after continuous electrolysis for 100 h [25]. The transmission electron microscopy (TEM) and powder X-ray diffraction (PXRD) tests revealed that the exchange of hydroxyl radicals with ligands occurred when the MOFs were immersed in the OER test system (1.0 M KOH). The *in-situ* reconstruction of FeNi-based MOF composites can form metal hydroxides on the surface. The origin of the catalytic activity from metal hydroxides was further confirmed by comparative experiments. The excellent catalytic activity was mainly due to the following results: (1) the low crystallinity of metal hydroxides provided abundant defective sites, thus exposing more active sites; (2) the octahedral structure of Fe-MOF could be well maintained, providing excellent dispersion of the metal hydroxides while effectively preventing agglomeration of active species during the long cycling test.

An in-depth understanding of the reconstruction mechanism, clarification of the activity origin, and exploitation of *in-situ* characterization techniques are necessary for the development of MOF-based OER electrocatalysts. Tang *et al*. [50] employed *in-situ* XAFS to elucidate the origin of OER catalytic activity at the atomic level (Figure 10b). The $Ni_{0.5}Co_{0.5}$-MOF-74 with a one-dimensional hexagonal pore was chosen as the object of study, and it was found that the metal junction of $Ni_{0.5}Co_{0.5}$-MOF-74 underwent two successive structural reconstructions during the OER process (Figure 10c–h). The first structural phase transition occurred in the low-potential region to form $Ni_{0.5}Co_{0.5}(OH)_2$, and then the second structural phase transition occurred in the high-

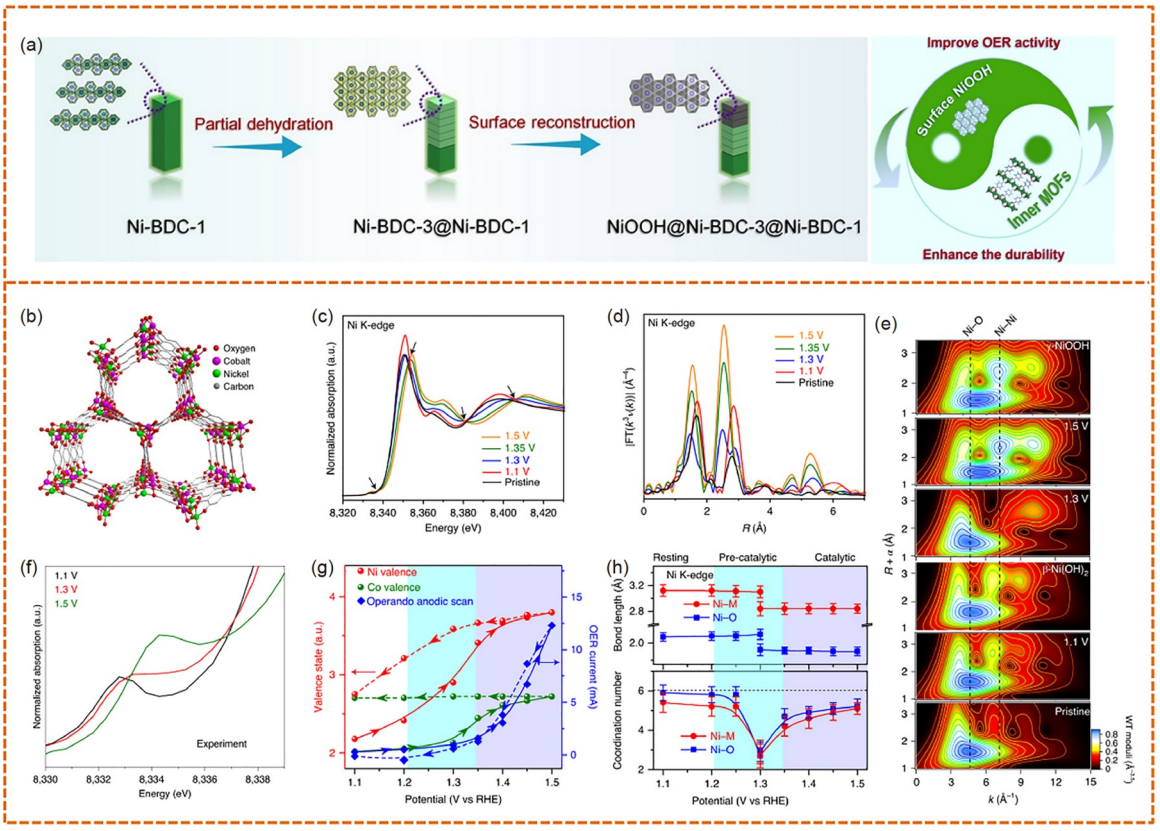

Figure 10 (a) Schematic illustration of the preparation of NiOOH@Ni-BDC-3@Ni-BDC-1. Reproduced with permission from Ref. [138], Copyright©2022 John Wiley & Sons, Inc. (b) Structural model of $Ni_{0.5}Co_{0.5}$-MOF-74. (c) XANES and (d) Fourier-transformed of Ni K-edge at different potentials. (e) Ni K-edge EXAFS WTs were recorded for the $Ni_{0.5}Co_{0.5}$-MOF-74 at different potentials. (f) The experimental pre-edge peaks of the Ni K-edge at 1.1, 1.3, and 1.5 V. (g) Valence states of Ni and Co, as well as the OER current as a function of applied potential. (h) Variation of bond length and coordination number of Ni–O and Ni–M coordination shells. Reproduced with permission from Ref. [50], Copyright©2020 Springer Nature (color online).

potential region to form the catalytically active species $Ni_{0.5}Co_{0.5}OOH_{0.75}$. The main contribution to the excellent catalytic activity of $Ni_{0.5}Co_{0.5}$-MOF-74 was due to the generation of $Ni_{0.5}Co_{0.5}OOH_{0.75}$ active species with enriched oxygen vacancies at high applied voltages, which enhanced $^{*}O$ adsorption. The authors also observed a "self-healing" phenomenon that $Ni_{0.5}Co_{0.5}$-MOF-74 could return to its original structure after 15 days in the air, suggesting that the reconstruction process in the OER process occurred locally at the metal nodes rather than in the dissociation of the MOF crystal structure.

It is noteworthy that although some of the MOF materials undergo partial reconstruction, the origin of catalytic activity is usually attributed to the metal hydroxides or hydroxyl oxides formed on the surface as well. Whether there are interactions between the metal hydroxides or hydroxyl oxides obtained from the reconstructions and the inner MOF structure without phase transformation, which affects the catalytic activity, has been rarely reported. Despite the occurrence of a partial phase change at the beginning of catalysis, a complete reconstruction of the catalyst may occur after continuous cycling tests [77].

4.2 Complete reconstruction

For catalysts where surface partial reconstructions occur, mostly based on large-size MOF structures, the active species generated by the surface reconstructions provide a degree of protection to the internal MOF structure. However, the general design principle of electrocatalysts shows that catalysts with smaller sizes or ultra-thin structures tend to expose more active sites and are therefore more sought after by researchers [139,140]. Subsequently, such MOF-based OER catalysts usually undergo complete reconstructions. In addition, previous studies have revealed that most MOF materials, particularly MOF based on carboxylic acid coordination, undergo reactions in alkaline solutions to dissociate ligands and *in-situ* form metal hydroxides [141]. Therefore, MOF-based OER catalysts may undergo partial surface reconstruction or complete *in-situ* reconstruction before the catalytic reaction occurred, which is often overlooked.

The Prussian blue analogue (PBA) and ZIF materials based on metal-nitrogen coordination are also widely used as OER catalysts due to their flexible adjustable metal centers and macroscopic structures. Zhang *et al*. [142] reported a novel NiFe PBA (NF-PBA) electrocatalyst. The electrochemical measurements showed that its performance stabilized after continuous electrolysis over 10 h activation, forming amorphous $Ni(OH)_2$ as active species (Figure 11a, b). *In-situ* XAFS was employed to precisely characterize the changes in Ni coordination number and Ni–O bond length during OER. In the low potential interval, some of the hydrogen atoms were removed from the hydroxyl groups in $Ni(OH)_2$, and some Ni^{2+} were oxidized to Ni^{3+} (NiO_2H_{2-x}). In the higher potential interval, NiO_2H_{1-x} containing Ni^{4+} was formed as the real active sites by the occurrence of successive deprotonation. These transition processes are reversible (Figure 11c). The excellent OER activity of this catalyst was mainly due to the fact that nickel ions in the amorphous system were more easily oxidized to higher valence states than that of the crystalline system, thereby exhibiting higher reactivity. Similarly, the Co/Mn-ZIF@Fe-Co-Mn PBA with a core-shell structure underwent complete structural reconstruction during the test, and the amorphous hydroxide obtained *via in-situ* translation drove the electrocatalytic process [143].

Fischer *et al*. [134] used a simple layer-by-layer deposition method to obtain a series of mixed-metal heterostructured MOFs. Those MOFs underwent the dissolution of organic ligands in alkaline solutions. The CV test further exacerbated their structural reconstruction to boost the formation of disordered NiFe hydroxides, whose abundant active site density drove efficient OER processes. The CV cycling tests matched with corresponding structural characterizations (PXRD, Fourier transform infrared, Raman, *etc.*) was used to determine the reconstruction process and extent (Figure 11d, e). Zhang *et al*. [144] synthesized a class of tri-metallic MOF materials at room temperature. Based on the flexible tunability of metals, the $(Ni_2Co_1)_{0.925}Fe_{0.075}$-MOF-NF delivered

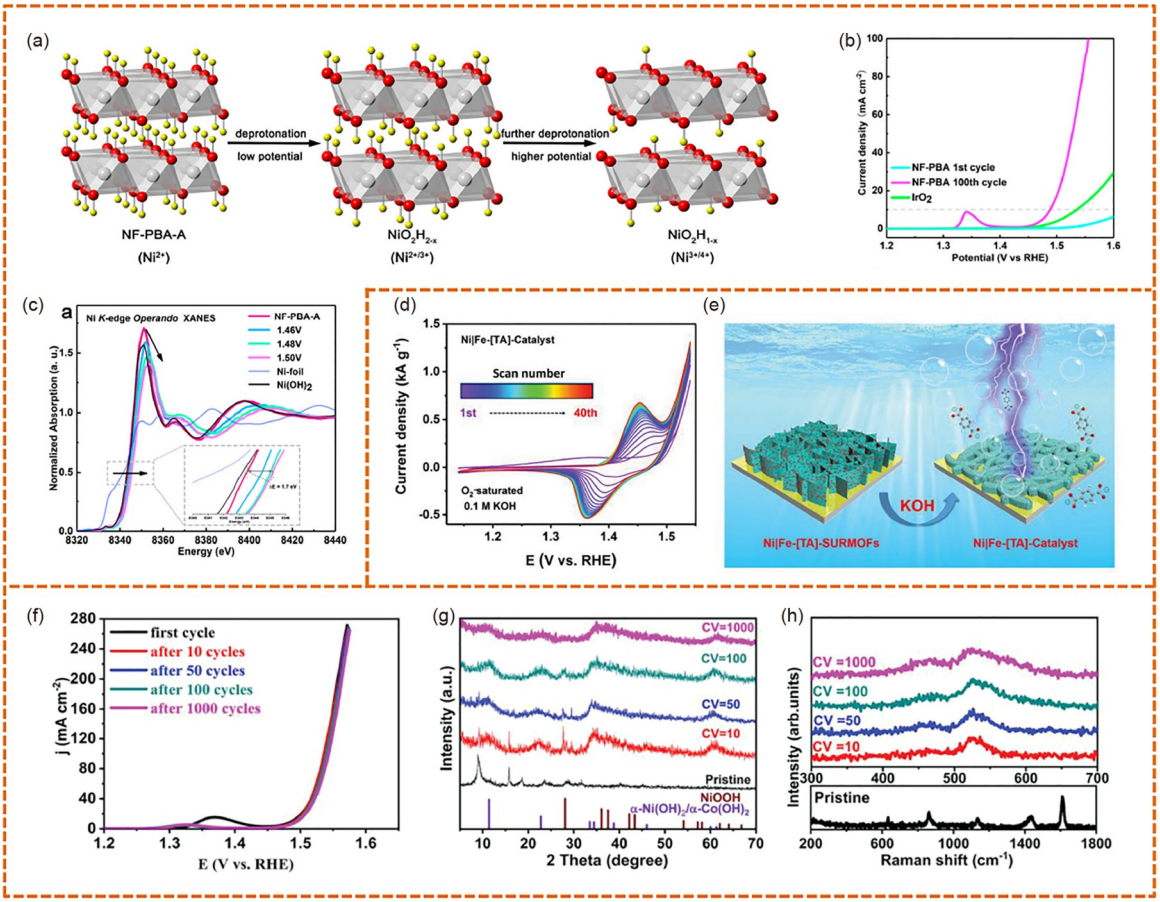

Figure 11 (a) Schematic diagram of the evolution of geometric and electronic of NiFe-PBA. (b) LSV curves of NF-PBA and IrO_2. (c) Operando Ni K-edge XANES of NF-PBA-A under different potentials. Reproduced with permission from Ref. [142], Copyright©2018 American Chemical Society. (d) CV curves of Ni|Fe-[TA]-catalyst electrode. (e) Schematic illustration of the transformation process of Ni|Fe-[TA]-SURMOFs. Reproduced with permission from Ref. [134], Copyright©2021 John Wiley & Sons, Inc. (f) LSV curves of $(Ni_2Co_1)_{0.925}Fe_{0.075}$-MOF-NF for different cycles. (g) XRD patterns, (h) Raman spectra of intermediates after different CV tests. Reproduced with permission from Ref. [144], Copyright©2019 John Wiley & Sons, Inc. (color online).

a low overpotential of 257 mV at 10 mA cm^{-2}. The structural evolution was investigated by observing the structures of intermediates after CV cycles. After 10 CV cycles, it was found that the LSV curves of $(Ni_2Co_1)_{0.925}Fe_{0.075}$-MOF-NF stabilized, and PXRD patterns and Raman spectra confirmed the transformation of the electrode materials from the initial MOF structure to the metal hydroxides active phase (Figure 11f–h).

4.3 Reconstruction effect

The reconstruction process mentioned above confirms that when MOFs were used as OER catalysts, most of them underwent partial or complete structural reconstructions to form the corresponding metal hydroxides that serve as the active driving phase during OER. However, these hydroxide/hydroxyl oxides usually exhibited distinguishable electrocatalytic properties. This was mainly owing to the reconstruction effects facilitated by different MOF structures and activation environments. Multiple factors can affect the nature (the structural composition, morphology, size, crystallinity, *etc.*) of the reconstructed products, such as the morphological properties of MOFs, the coordination environment of the metal, the preparation process of the working electrode, and the electrochemical activation mode and time, all of which in turn lead to different OER activities.

Lee *et al*. [49] first provided a systematic and comprehensive analysis regarding the effects of two typical electrochemical treatments (CV and amperometry methods) on the morphology and structure of the catalyst during the OER process. The ZIF-67 was selected as an object of study, combining *in-situ* UV-Vis spectroscopy, *in-situ* Raman spectroscopy, *ex-situ* transmission electron microscopy, PXRD, and other characterization tools. It was confirmed that ZIF-67 underwent several successive structural phase transitions during the OER process, which was mainly manifested by the conversion of ZIF-67 into α-$Co(OH)_2$ first, then β-$Co(OH)_2$, and finally further oxidation to form CoOOH as the active species. Among them, α-$Co(OH)_2$ can also be directly converted to CoOOH which has higher activity than CoOOH converted from β-$Co(OH)_2$ (Figure 12a, b). In addition, it was found that CV activation led to rapid dissociation of ZIF-67, while the amperometry provided a relatively stable state where the reconstruction proceeded steadily from the surface to the interior. Our group also prepared Co-MOF materials with different morphologies for OER electrocatalysts, which also underwent a multi-step reconstruction process from Co-MOF to $Co(OH)_2$ and then to CoOOH [145]. It was found that the binder (Nafion) used in the preparation of the working electrode had an important influence on the reconstruction process of Co-MOF. When the ultrathin Co-MOF with nanosheet structure was directly immersed into the alkaline solution, the highly crystalline alkaline decomposition product $Co(OH)_2$ was obtained as the active species. While the space site-block effect generated by the 3D structure of Nafion slowed down the alkaline decomposition process of Co-MOF, making the alkaline decomposition product $Co(OH)_2$ small size and low crystallinity, which delivered more active centers and consequently improved OER catalytic activity (Figure 12c). At the same time, activation by externally applied voltage also caused the reconstituted metal hydroxides with lower crystallinity, which was more prone to oxidation into high metal valence active centers.

Most of the dissociated organic ligands during structural reconstruction will be free in the electrolyte and can be reclaimed and reused by recrystallization. However, small amounts of dissociated ligands may be adsorbed on the surface or interlayer of the reconstructed product metal hydroxides due to charge or coordination interactions, which will affect the resulting OER activity. Li *et al*. [51] found that NiFe-MOFs underwent a structural reconstruction to form bimetallic hydroxides (NiFe LDHs) when used as OER catalysts, and some carboxylic acid ligands were adsorbed on the surface of NiFe LDHs, which played a crucial role in the enhancement of OER activity. As a Lewis base site, the carboxylic acid ligand can deliver the transport, activation, and dissociation of OH, which in turn optimized the adsorption strength of the reaction intermediates and promoted the reaction kinetics and catalytic activity of OER (Figure 12d). Our team and Sun's team [146,147] have similarly demonstrated the structural reconstruction of carboxylic acid-based MOF materials in the OER test system. The residual carboxylic acid ligands can act as proton relays to promote proton transfer in the electrocatalytic process, thereby reducing the OER reaction barrier.

4.4 Reconstruction as a reaction process

With in-depth research, the electrocatalysts structural reconstruction process of MOFs in alkaline electrolytes has been widely recognized. In addition to further study of the reconstruction effects, researchers have speculated that the structural transformation between MOFs and metal hydroxides can act as a promising strategy for preparing efficient OER electrocatalysts. First, the structures, metal types, and ligand components of MOFs are flexible and adjustable. Hence, MOFs can be used as a self-sacrificing template to achieve the directional regulation of morphology and structural composition of reconstructed products using a structural reconstruction strategy. Second, the structural reconstruction process of MOFs in alkaline electrolytes is simple and fast, which can be directly achieved in the electrocatalytic process. Furthermore, the MOF-derived metal hydroxides exhibit a large number of defects and abundant active sites, thereby giving rise to featured excellent elec-

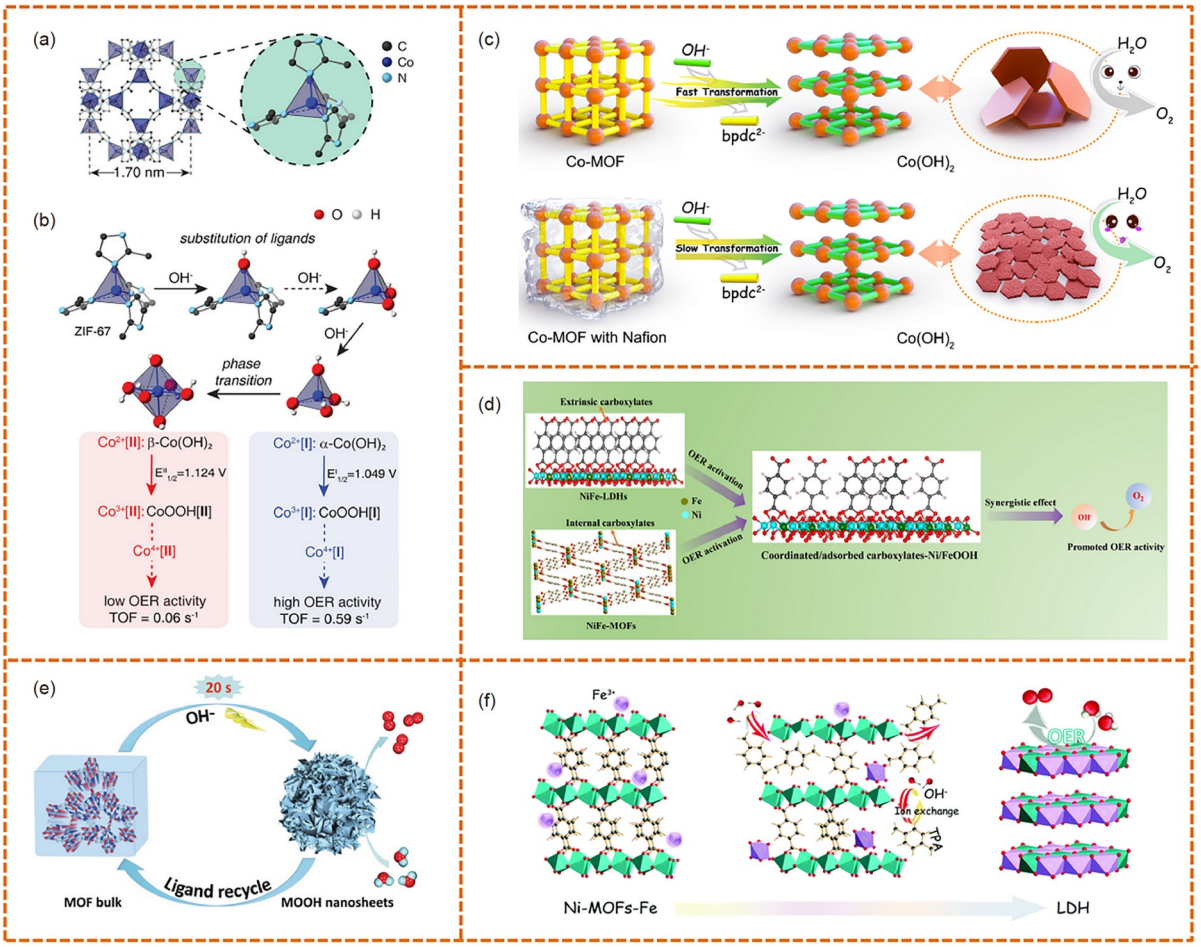

Figure 12 (a) Structural schematic diagrams of pristine ZIF-67. (b) Illustration of the evolution of ZIF-67 in alkaline electrolyte. Reproduced with permission from Ref. [49], Copyright©2019 American Chemical Society. (c) Schematic illustration of Nafion controlling the alkaline hydrolysis process. Reproduced with permission from Ref. [145], Copyright©2021 Springer Nature. (d) Schematic illustration of carboxylate promoting OER activity of metal hydroxides. Reproduced with permission from Ref. [51], Copyright©2021 John Wiley & Sons, Inc. (e) Schematic illustration of *in-situ* hydrolysis of bulk MOF into ultra-thin MOOH nanosheets using electric field assistance. Reproduced with permission from Ref. [148], Copyright©2020 John Wiley & Sons, Inc. (f) Schematic illustration of LDH formation through the ion exchange mechanism. Reproduced with permission from Ref. [149], Copyright©2022 Royal Society of Chemistry (color online).

trocatalytic activities. Finally, modulating the electronic structure of metal-active centers with residual ligand effects during the reconstruction of MOFs is an effective strategy to improve the activity of OER.

Therefore, the direct use of MOFs as OER catalysts in a strong alkaline electrolyte to obtain highly active catalytic species has been considered one of the most common methods for constructing efficient OER catalysts. Hong *et al.* [148] developed a new strategy for the rapid conversion of bulk MOF into ultrathin metal hydroxide nanosheets. An Fe-MOF (FJI-H25Fe), assembled from metal clusters $[Fe_3(\mu_3\text{-}O)(CH_3COO)_6]$ and 2,5-bis(1*H*-1,2,4-triazol-1-yl) terephthalic acid ligands, was prepared, and the sub-stable FJI-H25FeCo was obtained by partial Co substitution with Fe, where the weaker Co–O made FJI-H25FeCo rapid hydrolysis due to the attack of OH in the electrolyte. When two MOFs were immersed in KOH, they underwent some degree of hydrolysis, but the overall morphology remained unchanged. After being assisted with an applied electric field, the metastable FJI-H25FeCo was reconstructed from bulk structure to nanoflower assembled by nanosheets with a thickness of about 3 nm, and the active phases were composed of FeOOH, CoOOH, $(Fe_{0.67}Co_{0.33})OOH$, which exhibited excellent OER electrocatalytic activity (Figure 12e). The ligands initially coordinated with metals can also be recycled. This work also provided an interesting strategy to prepare metal hydroxides using MOF as a precursor template. Meanwhile, Liu *et al.* [149] first prepared lamellar Ni-MOFs with a negatively charged surface, followed by Fe cation-modified Ni-MOFs as OER pre-catalyst materials (Ni-MOFs-Fe) *via* electrostatic interactions. Based on the structural reconstruction effect of MOFs, Ni-Fe hydroxides

generated by the *in-situ* alkaline decomposition of Ni-MOFs-Fe in an alkaline solution were considered as the real active species, which gave the overpotential of 280 mV at 50 mA cm^{-2} (Figure 12f).

The role of ligands cannot be ignored regardless of whether structural reconstruction occurs. Fischer *et al*. [150] synthesized a series of bimetallic MOF materials ligated by carboxylic acid ligands with different functional groups. These MOFs could be converted into NiFe-based hydrogen oxide films by a simple one-step alkaline treatment. The organic ligands were partially retained within the NiFe-based hydrogen oxides. The different functional group modifications in the residual ligands stimulated the defect strain and modulated the reaction binding energy, and the catalyst containing amino-modified terephthalic acid ligands showed optimal OER activity, achieving a current density of 200 mA cm^{-2} at the low overpotential of only 210 mV.

Briefly, the structural reconstruction of MOF-based OER electrocatalysts mainly occurs in common carboxylic acid-based MOF, ZIF, and PBA materials. And the "discovery", "explanation", and "utilization" refer to the development process of the structural reconstruction mechanism, including the process from being detected, to being probed in depth, and then to being utilized as a strategy for the preparation of materials, respectively. Specifically, large numbers of developed MOF-based OER catalysts with excellent catalytic activities were identified as pre-catalysts for obtaining metal hydroxide/hydroxyl oxides to drive the OER process *via* one-step or multi-step structural reconstructions, which is referred to as "discovery" of structural reconstruction. Then, regarding the mechanism of the structural reconstruction of MOF-based OER catalysts into metal hydroxides, researchers have systematically investigated the factors influencing the structures of such metal hydroxides. It was confirmed that the metal hydroxides derived from alkaline reactions exhibited enhanced OER activities compared with conventional hydroxides, which can be attributed to the ligand effects and structural defects, referred to as the "explanation" of structural reconstruction. Finally, the structural reconstruction process was used as a promising method to prepare metal hydroxide catalysts using MOF materials with characteristic structures, compositions, and morphologies as self-sacrificing templates. Moreover, the design and performance optimizations of the target electrocatalysts can be achieved *via* modulating the alkaline decomposition process, which is referred to as the "utilization" of structural reconstruction.

5 Conclusions and perspectives

Benefiting from their flexible and adjustable nature in terms of compositions, pore environments, and distinct structural characteristics, various pristine MOF materials have been purposefully designed as excellent electrocatalysts for the OER process. This review focuses on the research progress of MOF materials utilized for efficient electrocatalytic OER and provides an updated assessment regarding their recent developments. Several common design strategies employed for MOF OER electrocatalysts are summarized, including the single metal MOFs with adjustable active centers, bimetallic/multi-metallic MOFs with intermetallic synergistic effects, conductive MOFs and substrate *in-situ* growth MOFs with excellent electron transfer abilities, amorphous MOFs and two-dimensional MOFs with rich active sites, as well as composite MOFs with multi-component functional integration. The optimization of OER performance in pristine MOFs has been achieved through atomic/molecular scale regulation. Particularly, the structural reconstruction of MOF materials during the electrocatalytic process is fully discussed, especially for those with weak alkali stability, including partial/complete structural reconstruction, factors influencing structural reconstruction, and the correlations among reconstruction products, pristine MOFs, and electrocatalytic activity. Last but not least, the reconstruction process can be employed as a strategy to prepare metal hydroxides with high OER activity using MOFs as precursors. Whilst significant efforts have been made and promising progress has been achieved in the engineering design of efficient and durable MOF electrocatalysts, there are still several challenges and opportunities that need to be addressed as follows:

(1) High stability. The well-defined structural properties of MOFs can facilitate the systematic analysis of their catalytic mechanisms and the establishment of structure-property relationships. Most reported MOF materials, which carboxylic acid-based MOFs in particular, exhibit poor stability under basic conditions. Consequently, they undergo multiple phase transitions either before or after the OER process. This lack of structural stability hampers the correlation between the original structural properties of MOFs and their electrocatalytic activity, making it challenging to analyze the catalytic mechanism effectively. Therefore, it becomes crucial to design rational ligands as well as coordination configurations to construct MOF catalysts with high alkali resistance stability. By leveraging the flexible coordination environment of metal centers and the tunable pore structure of MOF materials, the electronic structure of the active centers can be further optimized, thereby significantly improving the electrocatalytic performance.

(2) High conductivity. Achieving efficient electrocatalysis heavily relies on excellent charge transfer capability. However, the overall poor conductivity of MOF materials has always posed huge challenges, which therefore lead to the difficulty in constructing highly conductive MOF OER electrocatalysts. Designing conjugated ligands that bonded

to transition metals is a key strategy in enhancing the electrical conductivity of MOF materials. Conjugated ligands, such as hexa-aminobenzene, hexa-hydroxybenzene, hexa-mercaptobenzene, and hexa-hydroxytriphenylene, are commonly employed to coordinate with transition metals. The strong d-π interaction derived from the hybridization of the frontier orbitals of conjugated ligands and the d-orbitals of transition metals promotes the electron delocalization within the 2D plane, thus endowing the MOFs with narrow bandgaps and high intrinsic electrical conductivity. To date, only a few classic conjugated organic linkers and transition metals have been applied in constructing high-conductivity MOFs, which greatly limits the range and diversity of the research in this field. Hence, future efforts should focus on developing novel linkers and active sites with various coordination environments. Additionally, applying conductive substrates, such as NF, conductive carbon cloth, and titanium sheets, can also compensate for the defects caused by the low conductivity of MOFs.

(3) High current density and electrocatalytic activity. According to the International Energy Agency, hydrogen production by water electrolysis is predicted to hold a market share of approximately 22% by 2050. To achieve the industrial applications of electrocatalytic hydrolysis, a high current density (exceeding 1,000 mA cm^{-2}) with low overpotential is necessary. Generating a stable output of high current density necessitates the synergy of multiple aspects. Firstly, attaining high intrinsic activity primarily relies on the modulation of the electronic structure of the active centers. Secondly, employing suitable collectors is essential to facilitate efficient charge and mass transfer whilst minimizing secondary resistance caused by the binder. Moreover, those catalysts must exhibit substantial chemical and physical stabilities to prevent deactivation and detachment at elevated current densities, which leads to a decline in OER activity. Further, the cost of catalyst preparation should not be neglected, which encompasses both the expenses associated with raw materials as well as the processes involved in catalyst synthesis.

(4) Catalytic mechanism elucidation. MOF-based OER electrocatalysts can usually undergo partial or complete structural reconstructions. The metal active centers are susceptible to further oxidation during the OER process, which not only affects the catalytic performance but also makes the identification of active sites challenging. In particular, partial reconstruction can result in composite catalysts with more complicated structures and significant interfacial effects. Therefore, there is an urgent need to explore *in-situ* characterization techniques that can track those dynamic changes during the catalytic process. It is worth noting that each *in-situ* technique has its own working mechanism and application scope, which may limit the accuracy of the elucidated reaction mechanism. The integration of multiple advanced detection techniques (*e.g.*, *in-situ* TEM, Raman spectroscopy, Fourier transform infrared spectroscopy (FTIR), XAFS) is necessary to obtain more precise information on the morphological and electronic structure evolution of the catalysts. In addition, using DFT calculations to develop an accurate catalyst model can be immensely helpful in resolving the catalytic mechanism and clarifying the structure-property relationships, particularly for the reconstruction depth and multi-component synergy. These insights are essential for guiding the further design and optimization of OER electrocatalysts.

(5) Neutral electrolytic water. The main test environments for OER typically involve strong acids (pH 0, 1) or bases (pH 13, 14), and such electrolytes typically exhibit faster reaction kinetics to ensure low overpotential output at high current densities. However, working with such strong corrosive solutions imposes higher requirements on catalysts and collectors, which also greatly lifts the manufacturing cost. Therefore, it is vital yet challenging to develop catalysts with excellent activity under neutral electrolyte conditions. Furthermore, regarding the current condition of global freshwater scarcity, the development of highly active electrocatalysts for electrolytic seawater is of greater practical importance. The abundant Cl^- in seawater can accelerate the etching of catalysts and lead to poor stability, while the chlorine evolution reaction, as a competing reaction of OER, leads to the generation of toxic gases during the electrocatalytic process. Therefore, it is vital to develop Cl^- corrosion-resistant electrocatalysts. Furthermore, the improvement of OER selectivity through rational structural design is the key to realizing efficient seawater electrolysis. Such optimized catalysts are assembled into a two-electrode electrolyzer to obtain high current density, allowing for the assessment of their application potential under a neutral test environment.

Overall, despite numerous challenges, researchers have made considerable progress in the design and synthesis of MOF materials with efficient electrocatalytic OER performance. The inherent structural advantages of pristine MOFs, along with their structural reconstruction processes during OER, have provided new possibilities for enhancing OER performance. This present review provides great opportunities for further advances in the development of MOF materials for electrocatalysis, and hopefully serves as a comprehensive source to facilitate the industrialization of electrolytic water for hydrogen production.

Acknowledgements This work was supported by the National Natural Science Foundation of China (22035003, 21905142) and the Program of Introducing Talents of Discipline to Universities (B18030).

Conflict of interest The authors declare no conflict of interest.

1 Zhang K, Guo W, Liang Z, Zou R. *Sci China Chem*, 2019, 62: 417–429
2 Shinde SS, Jung JY, Wagh NK, Lee CH, Kim DH, Kim SH, Lee SU, Lee JH. *Nat Energy*, 2021, 6: 592–604
3 Subbaraman R, Tripkovic D, Chang KC, Strmcnik D, Paulikas AP, Hirunsit P, Chan M, Greeley J, Stamenkovic V, Markovic NM. *Nat Mater*, 2012, 11: 550–557
4 Luo J, Im JH, Mayer MT, Schreier M, Nazeeruddin MK, Park NG, Tilley SD, Fan HJ, Grätzel M. *Science*, 2014, 345: 1593–1596
5 Cheng C, Deng M, Li L, Wei Z. *Sci China Chem*, 2022, 65: 1854–1866
6 Tang YJ, Lan YQ. *Sci China Chem*, 2023, 66: 943–965
7 Wang Y, Kong B, Zhao D, Wang H, Selomulya C. *Nano Today*, 2017, 15: 26–55
8 Yang G, Yu S, Kang Z, Li Y, Bender G, Pivovar BS, Green Jr. JB, Cullen DA, Zhang F. *Adv Energy Mater*, 2020, 10: 1903871
9 Hunter BM, Gray HB, Müller AM. *Chem Rev*, 2016, 116: 14120–14136
10 Du J, Li F, Sun L. *Chem Soc Rev*, 2021, 50: 2663–2695
11 Kuznetsov DA, Naeem MA, Kumar PV, Abdala PM, Fedorov A, Müller CR. *J Am Chem Soc*, 2020, 142: 7883–7888
12 He Z, Zhang J, Gong Z, Lei H, Zhou D, Zhang N, Mai W, Zhao S, Chen Y. *Nat Commun*, 2022, 13: 2191
13 Yu D, Hao Y, Han S, Zhao S, Zhou Q, Kuo CH, Hu F, Li L, Chen HY, Ren J, Peng S. *ACS Nano*, 2023, 17: 1701–1712
14 Kou T, Li Y. *Sci China Chem*, 2022, 66: 301–303
15 Li S, Gao Y, Li N, Ge L, Bu X, Feng P. *Energy Environ Sci*, 2021, 14: 1897–1927
16 Zhang J, Zhang Q, Feng X. *Adv Mater*, 2019, 31: 1808167
17 Zhou X, Jin H, Xia BY, Davey K, Zheng Y, Qiao S. *Adv Mater*, 2021, 33: 2104341
18 Bao T, Zou Y, Zhang C, Yu C, Liu C. *Angew Chem Int Ed*, 2022, 61: e202209433
19 Liu Y, Wang Y, Zhao S, Tang Z. *Small Methods*, 2022, 6: 2200773
20 Zhong M, Liu M, Li N, Bu XH. *J Energy Chem*, 2021, 63: 113–129
21 Kong L, Zhong M, Shuang W, Xu Y, Bu XH. *Chem Soc Rev*, 2020, 49: 2378–2407
22 Shan J, Ye C, Zhu C, Dong J, Xu W, Chen L, Jiao Y, Jiang Y, Song L, Zhang Y, Jaroniec M, Zhu Y, Zheng Y, Qiao SZ. *J Am Chem Soc*, 2022, 144: 23214–23222
23 Wei YS, Zhang M, Zou R, Xu Q. *Chem Rev*, 2020, 120: 12089–12174
24 Xiao Z, Mei Y, Yuan S, Mei H, Xu B, Bao Y, Fan L, Kang W, Dai F, Wang R, Wang L, Hu S, Sun D, Zhou HC. *ACS Nano*, 2019, 13: 7024–7030
25 Liu M, Kong L, Wang X, He J, Bu X. *Small*, 2019, 15: 1903410
26 Duan J, Chen S, Zhao C. *Nat Commun*, 2017, 8: 15341
27 Liu Y, Wang S, Li Z, Chu H, Zhou W. *Coord Chem Rev*, 2023, 484: 215117
28 Lin R, Li X, Krajnc A, Li Z, Li M, Wang W, Zhuang L, Smart S, Zhu Z, Appadoo D, Harmer JR, Wang Z, Buzanich AG, Beyer S, Wang L, Mali G, Bennett TD, Chen V, Hou J. *Angew Chem Int Ed*, 2022, 61: e202112880
29 Wang Y, Zhao L, Ma J, Zhang J. *Energy Environ Sci*, 2022, 15: 3830–3841
30 Man IC, Su H, Calle-Vallejo F, Hansen HA, Martínez JI, Inoglu NG, Kitchin J, Jaramillo TF, Nørskov JK, Rossmeisl J. *ChemCatChem*, 2011, 3: 1159–1165
31 Grimaud A, May KJ, Carlton CE, Lee YL, Risch M, Hong WT, Zhou J, Shao-Horn Y. *Nat Commun*, 2013, 4: 2439
32 Tao HB, Fang L, Chen J, Yang HB, Gao J, Miao J, Chen S, Liu B. *J Am Chem Soc*, 2016, 138: 9978–9985
33 Grimaud A, Hong WT, Shao-Horn Y, Tarascon JM. *Nat Mater*, 2016, 15: 121–126
34 Suntivich J, May KJ, Gasteiger HA, Goodenough JB, Shao-Horn Y. *Science*, 2011, 334: 1383–1385
35 Gao L, Cui X, Sewell CD, Li J, Lin Z. *Chem Soc Rev*, 2021, 50: 8428–8469
36 Yoo JS, Rong X, Liu Y, Kolpak AM. *ACS Catal*, 2018, 8: 4628–4636
37 Wang C, Zhai P, Xia M, Wu Y, Zhang B, Li Z, Ran L, Gao J, Zhang X, Fan Z, Sun L, Hou J. *Angew Chem Int Ed*, 2021, 60: 27126–27134
38 Song J, Wei C, Huang ZF, Liu C, Zeng L, Wang X, Xu ZJ. *Chem Soc Rev*, 2020, 49: 2196–2214
39 Zhang N, Chai Y. *Energy Environ Sci*, 2021, 14: 4647–4671
40 Wang X, Xi S, Huang P, Du Y, Zhong H, Wang Q, Borgna A, Zhang YW, Wang Z, Wang H, Yu ZG, Lee WSV, Xue J. *Nature*, 2022, 611: 702–708
41 Lin C, Li JL, Li X, Yang S, Luo W, Zhang Y, Kim SH, Kim DH, Shinde SS, Li YF, Liu ZP, Jiang Z, Lee JH. *Nat Catal*, 2021, 4: 1012–1023
42 Song XZ, Zhang N, Wang XF, Tan Z. *Mater Today Energy*, 2021, 19: 100597
43 Kollmannsberger KL, Kronthaler L, Jinschek JR, Fischer RA. *Chem Soc Rev*, 2022, 51: 9933–9959
44 Peng Y, Sanati S, Morsali A, García H. *Angew Chem Int Ed*, 2023, 62: e202214707
45 Jahan M, Liu Z, Loh KP. *Adv Funct Mater*, 2013, 23: 5363–5372
46 Zhao S, Wang Y, Dong J, He CT, Yin H, An P, Zhao K, Zhang X, Gao C, Zhang L, Lv J, Wang J, Zhang J, Khattak AM, Khan NA, Wei Z, Zhang J, Liu S, Zhao H, Tang Z. *Nat Energy*, 2016, 1: 16184
47 Zhao L, Dong B, Li S, Zhou L, Lai L, Wang Z, Zhao S, Han M, Gao K, Lu M, Xie X, Chen B, Liu Z, Wang X, Zhang H, Li H, Liu J, Zhang H, Huang X, Huang W. *ACS Nano*, 2017, 11: 5800–5807
48 Huang J, Li Y, Huang R, He C, Gong L, Hu Q, Wang L, Xu Y, Tian X, Liu S, Ye Z, Wang F, Zhou D, Zhang W, Zhang J. *Angew Chem Int Ed*, 2018, 57: 4632–4636
49 Zheng W, Liu M, Lee LYS. *ACS Catal*, 2019, 10: 81–92
50 Zhao S, Tan C, He CT, An P, Xie F, Jiang S, Zhu Y, Wu KH, Zhang B, Li H, Zhang J, Chen Y, Liu S, Dong J, Tang Z. *Nat Energy*, 2020, 5: 881–890
51 Li C, Zhao J, Xie L, Wu J, Ren Q, Wang Y, Li G. *Angew Chem Int Ed*, 2021, 60: 18129–18137
52 Lyu S, Guo C, Wang J, Li Z, Yang B, Lei L, Wang L, Xiao J, Zhang T, Hou Y. *Nat Commun*, 2022, 13: 6171
53 Liu Y, Li X, Zhang S, Wang Z, Wang Q, He Y, Huang W, Sun Q, Zhong X, Hu J, Guo X, Lin Q, Li Z, Zhu Y, Chueh C, Chen C, Xu Z, Zhu Z. *Adv Mater*, 2023, 35: 2300945
54 Wang H, Zhang X, Yin F, Chu W, Chen B. *J Mater Chem A*, 2020, 8: 22111–22123
55 Bagchi D, Phukan N, Sarkar S, Das R, Ray B, Bellare P, Ravishankar N, Peter SC. *J Mater Chem A*, 2021, 9: 9319–9326
56 Kang J, Lee MJ, Oh NG, Shin J, Kwon SJ, Chun H, Kim SJ, Yun H, Jo H, Ok KM, Do J. *Chem Mater*, 2021, 33: 2804–2813
57 He F, Zhao Y, Yang X, Zheng S, Yang B, Li Z, Kuang Y, Zhang Q, Lei L, Qiu M, Dai L, Hou Y. *ACS Nano*, 2022, 16: 9523–9534
58 Sekar P, Vasanthakumar P, Shanmugam R, Senthil Kumar S, Agnoli S, Deepak RJ, Murugan K, Bhuvanesh N, Karvembu R. *Green Chem*, 2022, 24: 9233–9244
59 Liang J, Gao X, Guo B, Ding Y, Yan J, Guo Z, Tse ECM, Liu J. *Angew Chem Int Ed*, 2021, 60: 12770–12774
60 Seal N, Karmakar A, Kundu S, Neogi S. *ACS Sustain Chem Eng*, 2022, 11: 979–993
61 Qi L, Su YQ, Xu Z, Zhang G, Liu K, Liu M, Hensen EJM, Lin RYY. *J Mater Chem A*, 2020, 8: 22974–22982
62 Ai L, Luo Y, Huang W, Tian Y, Jiang J. *Int J Hydrogen Energy*, 2022, 47: 12893–12902
63 Cheng W, Wu Z, Luan D, Zang S, Lou XWD. *Angew Chem Int Ed*, 2021, 60: 26397–26402
64 Shahbazi Farahani F, Rahmanifar MS, Noori A, El-Kady MF, Hassani N, Neek-Amal M, Kaner RB, Mousavi MF. *J Am Chem Soc*, 2022, 144: 3411–3428
65 Kong Y, Xiong D, Lu C, Wang J, Liu T, Ying S, Ma X, Yi FY. *ACS Appl Mater Interfaces*, 2022, 14: 37804–37813
66 Yu L, Xiao J, Huang C, Zhang Z, Qiu M, Yu Y, Wang Y, Yu JC. *J*

Mater Chem A, 2022, 10: 17552–17560
67 Li S, Wang T, Tang D, Yang Y, Tian Y, Cui F, Sun J, Jing X, Sholl DS, Zhu G. *Adv Sci*, 2022, 9: 2203712
68 Zhao H, Yu L, Zhang L, Dai L, Yao F, Huang Y, Sun J, Zhu J. *ACS Sustain Chem Eng*, 2021, 9: 10892–10901
69 Li C, Xie L, Zhao J, Gu L, Tang H, Zheng L, Li G. *Angew Chem Int Ed*, 2022, 61: e202116934
70 Wang S, Li Q, Sun S, Ge K, Zhao Y, Yang K, Zhang Z, Cao J, Lu J, Yang Y, Zhang Y, Pan M, Lin Z, Zhu L. *J Mater Chem A*, 2022, 10: 5350–5360
71 An H, Hu Y, Song N, Mu T, Bai S, Peng Y, Liu L, Tang Y. *Chem Sci*, 2022, 13: 3035–3044
72 Sun D, Wong LW, Wong HY, Lai KH, Ye L, Xv X, Ly TH, Deng Q, Zhao J. *Angew Chem Int Ed*, 2023, 62: e202216008
73 Li F, Jiang M, Lai C, Xu H, Zhang K, Jin Z. *Nano Lett*, 2022, 22: 7238–7245
74 Yu H, Wang L, Li H, Luo Z, Isimjan TT, Yang X. *Chem Eur J*, 2022, 28: 2201784
75 Hu F, Yu D, Zeng W, Lin Z, Han S, Sun Y, Wang H, Ren J, Hung S, Li L, Peng S. *Adv Energy Mater*, 2023, 13: 2301224
76 Zhao S, Deng L, Xiong Y, Hu F, Yin L, Yu D, Li LL, Peng S. *Sci China Mater*, 2023, 66: 1373–1382
77 Wang CP, Feng Y, Sun H, Wang Y, Yin J, Yao Z, Bu XH, Zhu J. *ACS Catal*, 2021, 11: 7132–7143
78 Raja SD, Lin H-W, Lu S-Y. *Nano Energy*, 2019, 57: 1-13
79 Feng K, Zhang D, Liu F, Li H, Xu J, Xia Y, Li Y, Lin H, Wang S, Shao M, Kang Z, Zhong J. *Adv Energy Mater*, 2020, 10: 2000184
80 Senthil Raja D, Huang CL, Chen YA, Choi YM, Lu SY. *Appl Catal B-Environ*, 2020, 279: 119375
81 Yang G, Zhu J, Yuan P, Hu Y, Qu G, Lu BA, Xue X, Yin H, Cheng W, Cheng J, Xu W, Li J, Hu J, Mu S, Zhang JN. *Nat Commun*, 2021, 12: 1734
82 Bai Y, Zhang G, Zheng S, Li Q, Pang H, Xu Q. *Sci China Mater*, 2020, 64: 137–148
83 Cheng W, Xi S, Wu ZP, Luan D, Lou XWD. *Sci Adv*, 2021, 7: eabk0919
84 Han Z, Yan Z, Wang K, Kang X, Lv K, Zhang X, Zhou Z, Yang S, Shi W, Cheng P. *Sci China Chem*, 2022, 65: 1088–1093
85 Subramanian BT, Thomas S, Gumpu MB, Biju VMN. *J Electroanal Chem*, 2022, 925: 116904
86 Lu XF, Liao PQ, Wang JW, Wu JX, Chen XW, He CT, Zhang JP, Li GR, Chen XM. *J Am Chem Soc*, 2016, 138: 8336–8339
87 Tao L, Lin CY, Dou S, Feng S, Chen D, Liu D, Huo J, Xia Z, Wang S. *Nano Energy*, 2017, 41: 417–425
88 Shan J, Ye C, Jiang Y, Jaroniec M, Zheng Y, Qiao SZ. *Sci Adv*, 2022, 8: eabo0762
89 Zhao Y, Lu XF, Wu Z, Pei Z, Luan D, Lou XWD. *Adv Mater*, 2023, 35: e2207888
90 Yao Y, Ma Z, Dou Y, Lim SY, Zou J, Stamate E, Jensen JO, Zhang W. *Chem Eur J*, 2022, 28: 2104288
91 Zhang M, Xu W, Li T, Zhu H, Zheng Y. *Inorg Chem*, 2020, 59: 15467–15477
92 Li Y, Zhao T, Lu M, Wu Y, Xie Y, Xu H, Gao J, Yao J, Qian G, Zhang Q. *Small*, 2019, 15: 1901940
93 Wang XL, Dong LZ, Qiao M, Tang YJ, Liu J, Li Y, Li SL, Su JX, Lan YQ. *Angew Chem Int Ed*, 2018, 57: 9660–9664
94 Cheng W, Lu XF, Luan D, Lou XWD. *Angew Chem Int Ed*, 2020, 59: 18234–18239
95 Kandambeth S, Kale VS, Fan D, Bau JA, Bhatt PM, Zhou S, Shkurenko A, Rueping M, Maurin G, Shekhah O, Eddaoudi M. *Adv Energy Mater*, 2023, 13: 2202964
96 Li Y, Wu Y, Li T, Lu M, Chen Y, Cui Y, Gao J, Qian G. *Carbon Energy*, 2023, 5: 265
97 Liu D, Xu H, Wang C, Shang H, Yu R, Wang Y, Li J, Li X, Du Y. *Inorg Chem*, 2021, 60: 5882–5889
98 Zhang W, Wang Y, Zheng H, Li R, Tang Y, Li B, Zhu C, You L, Gao MR, Liu Z, Yu SH, Zhou K. *ACS Nano*, 2020, 14: 1971–1981
99 Wang Y, Yan L, Dastafkan K, Zhao C, Zhao X, Xue Y, Huo J, Li S, Zhai Q. *Adv Mater*, 2021, 33: 2006351
100 Gutiérrez-Tarriño S, Olloqui-Sariego JL, Calvente JJ, Espallargas GM, Rey F, Corma A, Oña-Burgos P. *J Am Chem Soc*, 2020, 142: 19198–19208
101 Ye B, Jiang R, Yu Z, Hou Y, Huang J, Zhang B, Huang Y, Zhang Y, Zhang R. *J Catal*, 2019, 380: 307–317
102 Guo C, Jiao Y, Zheng Y, Luo J, Davey K, Qiao SZ. *Chem*, 2019, 5: 2429–2441
103 Song D, Guo H, Huang K, Zhang H, Chen J, Wang L, Lian C, Wang Y. *Mater Today*, 2022, 54: 42–51
104 Ko M, Mendecki L, Mirica KA. *Chem Commun*, 2018, 54: 7873–7891
105 Wang A, Niu H, Wang X, Wan X, Xie L, Zhang Z, Wang J, Guo Y. *J Mater Chem A*, 2022, 10: 13005–13012
106 Wei X, Cao S, Xu H, Jiang C, Wang Z, Ouyang Y, Lu X, Dai F, Sun D. *ACS Mater Lett*, 2022, 4: 1991–1998
107 Zhao M, Huang Y, Peng Y, Huang Z, Ma Q, Zhang H. *Chem Soc Rev*, 2018, 47: 6267–6295
108 Jia H, Yao Y, Zhao J, Gao Y, Luo Z, Du P. *J Mater Chem A*, 2018, 6: 1188–1195
109 Li J, Liu P, Mao J, Yan J, Song W. *J Mater Chem A*, 2021, 9: 1623–1629
110 Liu XH, Yang YW, Liu XM, Hao Q, Wang LM, Sun B, Wu J, Wang D. *Langmuir*, 2020, 36: 7528–7532
111 Xing D, Wang Y, Zhou P, Liu Y, Wang Z, Wang P, Zheng Z, Cheng H, Dai Y, Huang B. *Appl Catal B-Environ*, 2020, 278: 119295
112 Li J, Liu P, Mao J, Yan J, Song W. *J Mater Chem A*, 2021, 9: 11248–11254
113 Li WH, Lv J, Li Q, Xie J, Ogiwara N, Huang Y, Jiang H, Kitagawa H, Xu G, Wang Y. *J Mater Chem A*, 2019, 7: 10431–10438
114 Sun F, Wang G, Ding Y, Wang C, Yuan B, Lin Y. *Adv Energy Mater*, 2018, 8: 1800584
115 Cao C, Ma D, Xu Q, Wu X, Zhu Q. *Adv Funct Mater*, 2018, 29: 1807418
116 Li DJ, Li QH, Gu ZG, Zhang J. *J Mater Chem A*, 2019, 7: 18519–18528
117 Chen G, Zhang J, Wang F, Wang L, Liao Z, Zschech E, Müllen K, Feng X. *Chem Eur J*, 2018, 24: 18413–18418
118 Wu H, Huang S, Ding F, Ma Y, Zhai Q, Ren Y, Yang Y, Chen L, Tang S, Meng X. *J Phys Chem C*, 2022, 126: 19715–19725
119 Dang Y, Han P, Li Y, Zhang Y, Zhou Y. *J Mater Sci*, 2020, 55: 13951–13963
120 Li J, Huang W, Wang M, Xi S, Meng J, Zhao K, Jin J, Xu W, Wang Z, Liu X, Chen Q, Xu L, Liao X, Jiang Y, Owusu KA, Jiang B, Chen C, Fan D, Zhou L, Mai L. *ACS Energy Lett*, 2018, 4: 285–292
121 Hou X, Han Z, Xu X, Sarker D, Zhou J, Wu M, Liu Z, Huang M, Jiang H. *Chem Eng J*, 2021, 418: 129330
122 Dai S, Liu Y, Mei Y, Hu J, Wang K, Li Y, Jin N, Wang X, Luo H, Li W. *Dalton Trans*, 2022, 51: 15446–15457
123 Wu H, Zhai Q, Ding F, Sun D, Ma Y, Ren Y, Wang B, Li F, Bian H, Yang Y, Chen L, Tang S, Meng X. *Dalton Trans*, 2022, 51: 14306–14316
124 Zhao M, Wang Y, Ma Q, Huang Y, Zhang X, Ping J, Zhang Z, Lu Q, Yu Y, Xu H, Zhao Y, Zhang H. *Adv Mater*, 2015, 27: 7372–7378
125 Li F, Wang P, Huang X, Young DJ, Wang H, Braunstein P, Lang J. *Angew Chem Int Ed*, 2019, 58: 7051–7056
126 Zhao M, Guo T, Qian W, Wang Z, Zhao X, Wen L, He D. *Chem Eng J*, 2021, 422: 130055
127 Hai G, Jia X, Zhang K, Liu X, Wu Z, Wang G. *Nano Energy*, 2018, 44: 345–352
128 Yang X, Zhang J, Tian X, Qin J, Zhang X, Ma L. *Angew Chem Int Ed*, 2023, 62: e202216699
129 Jin S. *ACS Energy Lett*, 2017, 2: 1937–1938
130 Liu D, Ai H, Li J, Fang M, Chen M, Liu D, Du X, Zhou P, Li F, Lo KH, Tang Y, Chen S, Wang L, Xing G, Pan H. *Adv Energy Mater*, 2020, 10: 2002464

131 Xu ZJ. *Sci China Mater*, 2019, 63: 3-7
132 Miles DO, Jiang D, Burrows AD, Halls JE, Marken F. *Electrochem Commun*, 2013, 27: 9–13
133 Zheng W, Lee LYS. *ACS Energy Lett*, 2021, 6: 2838–2843
134 Hou S, Li W, Watzele S, Kluge RM, Xue S, Yin S, Jiang X, Döblinger M, Welle A, Garlyyev B, Koch M, Müller-Buschbaum P, Wöll C, Bandarenka AS, Fischer RA. *Adv Mater*, 2021, 33: 2103218
135 Selvam NCS, Du L, Xia BY, Yoo PJ, You B. *Adv Funct Mater*, 2020, 31: 2008190
136 Wang X, Li B, Wu YP, Tsamis A, Yu HG, Liu S, Zhao J, Li YS, Li DS. *Inorg Chem*, 2020, 59: 4764–4771
137 Li W, Watzele S, El-Sayed HA, Liang Y, Kieslich G, Bandarenka AS, Rodewald K, Rieger B, Fischer RA. *J Am Chem Soc*, 2019, 141: 5926–5933
138 Zhang L, Wang J, Jiang K, Xiao Z, Gao Y, Lin S, Chen B. *Angew Chem Int Ed*, 2022, 61: e202214794
139 Lee MK, Shokouhimehr M, Kim SY, Jang HW. *Adv Energy Mater*, 2022, 12: 2003990
140 Sakamoto R, Fukui N, Maeda H, Toyoda R, Takaishi S, Tanabe T, Komeda J, Amo-Ochoa P, Zamora F, Nishihara H. *Coord Chem Rev*, 2022, 472: 214787
141 Zhang H, Xu B, Mei H, Mei Y, Zhang S, Yang Z, Xiao Z, Kang W, Sun D. *Small*, 2019, 15: 1904663
142 Su X, Wang Y, Zhou J, Gu S, Li J, Zhang S. *J Am Chem Soc*, 2018, 140: 11286–11292
143 Zhang Q, Wang H, Han W, Yang L, Zhang Y, Bai Z. *Nano Res*, 2023, 16: 3695–3702
144 Qian Q, Li Y, Liu Y, Yu L, Zhang G. *Adv Mater*, 2019, 31: 1901139
145 Liu M, Kong L, Wang X, He J, Zhang J, Zhu J, Bu XH. *Nano Res*, 2021, 14: 4680–4688
146 Li W, Li F, Yang H, Wu X, Zhang P, Shan Y, Sun L. *Nat Commun*, 2019, 10: 5074
147 Liu M, Li N, Wang X, Zhao J, Zhong D, Li W, Bu X. *Angew Chem Int Ed*, 2023, 62: e202300507
148 Tian J, Jiang F, Yuan D, Zhang L, Chen Q, Hong M. *Angew Chem Int Ed*, 2020, 59: 13101–13108
149 Wang X, Wang X, Zhao L, Zhang H, Liu M, Zhang C, Liu S. *Inorg Chem Front*, 2022, 9: 179–185
150 Li W, Xue S, Watzele S, Hou S, Fichtner J, Semrau AL, Zhou L, Welle A, Bandarenka AS, Fischer RA. *Angew Chem Int Ed*, 2020, 59: 5837–5843